A MULTIPARAMETRIC QUANTITATIVE MRI PIPELINE FOR PRECLINICAL APPLICATIONS

by

Belal TAVASHI

B.S., in Biomedical Engineering, Ankara University, 2022

Submitted to the Institute of Biomedical Engineering
in partial fulfillment of the requirements
for the degree of
Master of Science
in
Biomedical Engineering

Boğaziçi University
2025

A MULTIPARAMETRIC QUANTITATIVE MRI PIPELINE FOR PRECLINICAL APPLICATIONS

APPROVED BY:

Assist. Prof. Dr. Pınar Senay Özbay .....
(Thesis Advisor)

Prof. Dr. Esin Öztürk Işık .....

Assoc. Prof. Dr. Emine Ülkü Sarıtaş .....

DATE OF APPROVAL: 25 August 2025

ACKNOWLEDGMENTS

This work is based on data acquired as part of the TÜBİTAK 1004 project (Grant Number: 22AG016). I gratefully acknowledge this support.

I would first like to express my deepest gratitude to my advisor, **Dr. Pınar Senay Özbay**, for her guidance, patience, and encouragement throughout this journey. Her mentorship has been invaluable, not only in shaping this thesis but also in shaping the way I think as a researcher. I am also thankful to **Dr. Esin Öztürk Işık** and all other faculty members and colleagues in our institute who generously shared their expertise and offered advice whenever I needed direction. I am also grateful to my lab mates and teammates in **the MIMLAB team**. Their insights, discussions, and friendship in the lab provided not only academic support but also a sense of community during challenging times.

I am sincerely grateful to my lovely, amazing friends—**Yağmur**, **Kübra**, **Berrah**, **Muhammad Bin Sanaullah**, **Atilla**, **Cem**, **Berat** and **Elif**—who accompanied me in both the struggles and the joys of these years, shared in the existential questioning and philosophical discussions, and even tolerated my endless dad jokes (sometimes laughing at them). They stood by me through late nights, setbacks, and countless conversations, making the journey lighter.

To my family—my mom Sahar, my dad Abdulhadi, and my siblings Hajar, Bayan, Al-Harith, and Maria—I owe more than words can express. With them, I endured the challenges of a difficult forced immigration, and with them, I found the resilience to continue. Their love and unwavering belief in me carried me through hardships I would not have faced alone.

Finally, I would like to thank my partner, **Yağmur**. Your love and patience carried me through the hardest parts of this work and shaped the way I grew along the way. I still remember when you once shared with me Can Yücel's words from his poem "*Her şey sende gizli*" — everything is hidden within you. At the time, those words gave me strength when I needed it most, and they continue to remind me of how much of this journey I owe to you. And just as he says "*Sevdiklerin kadar iyisin*"—"you are only as good as those you love"—I feel lucky to have you by my side as I grew. This work is yours as much as it is mine.

ACADEMIC ETHICS AND INTEGRITY STATEMENT

I, Belal TAVASHI, hereby certify that I am aware of the Academic Ethics and Integrity Policy issued by the Council of Higher Education (YÖK) and I fully acknowledge all the consequences due to its violation by plagiarism or any other way.

Name :

Signature:

Date:

ABSTRACT

A MULTIPARAMETRIC QUANTITATIVE MRI PIPELINE FOR PRECLINICAL APPLICATIONS

Quantitative MRI (qMRI) enables direct measurement of tissue properties - such as relaxation times and magnetic susceptibility- that shape the MRI signal in predictable ways. Unlike qualitative contrasts, qMRI provides reproducible biomarkers for studying processes from healthy aging to neurodegenerative and psychiatric disorders, with multiparametric approaches offering complementary insights as each parameter reflects distinct biological features. This thesis presents a multiparametric qMRI pipeline for preclinical use, demonstrated on 21 female Wistar rats at 7T. The pipeline integrates relaxometry mapping (T_1, T_2, R_2^*) within a Python-based framework featuring a GUI for subject-level analysis, and ensures reproducibility through automated conversion of raw data into BIDS-compliant format. Relaxometry maps were benchmarked against existing toolboxes with Bland-Altman analysis, confirming strong agreement. The pipeline was further extended to quantitative susceptibility mapping (QSM), where a dedicated phantom enabled evaluation of reconstruction algorithms; STAR-QSM outperformed alternatives by visual and nRMSE assessment and was adopted for preprocessing phase data and generating susceptibility maps with the Sepia toolbox. Regional mean susceptibility and relaxometry measures were extracted, with ROI-level mean, standard deviation, SEM, and voxel counts reported for transparency. Overall, this work establishes a reproducible preclinical qMRI framework unifying relaxometry and QSM, demonstrating methodological rigor and translational potential while providing a foundation for future studies of microstructural and physiological changes in disease and aging models.

Keywords: Magnetic Resonance Imaging, T_1, T_2, R_2^*, QSM, Preclinical, Wistar Rats, qMRI, Brain.

ÖZET

PREKLİNİK UYGULAMALARA YÖNELİK ÇOK PARAMETRELİ NİCEL MRG HARİTALAMA VE İŞLEME HATTI

Kantitatif manyetik rezonans görüntüleme (qMRI), relaksasyon süreleri ve manyetik duyarlılık gibi MRI sinyalini öngörülebilir biçimde etkileyen dokuya özgü özelliklerin doğrudan ölçülmesini sağlayarak nitel kontrastların ötesinde tekrarlanabilir biyogöstergeler sunar. Böylece, sağlıklı yaşlanmadan psikiyatrik bozukluklara kadar geniş bir yelpazedeki süreçler incelenebilir; çoklu parametrelerin birlikte değerlendirilmesi ise her birinin farklı biyolojik özellikleri yansıtması sayesinde tamamlayıcı bir bakış açısı sağlar. Bu tez kapsamında, preklinik uygulamalara yönelik çok parametreli bir qMRI işlem hattı geliştirilmiş ve 7T tarayıcıda görüntülenen 21 dişi Wistar sıçanı üzerinde uygulanmıştır. İşlem hattı, relaksometri haritalarının (T_1, T_2, R_2^*) çıkarılmasını, Python tabanlı bir çerçeve ve kullanıcı dostu bir GUI'yi içermekte; yeniden üretilebilirlik için verileri otomatik olarak BIDS uyumlu formata dönüştürmektedir. Elde edilen relaksometri haritaları mevcut yazılımlarla Bland-Altman analizi kullanılarak karşılaştırılmış ve yüksek uyum göstermiştir. İşlem hattı ayrıca kantitatif manyetik duyarlılık haritalamasına (QSM) genişletilmiş; özel oluşturulan fantom ile algoritmalar karşılaştırılmış ve STAR-QSM görsel inceleme ile nRMSE analizlerinde en başarılı yöntem olarak belirlenmiştir. Bu yöntem, faz verilerinin ön işlenmesinde ve duyarlılık haritalarının Sepia yazılımı aracılığıyla üretilmesinde kullanılmıştır. Tüm ROI'ler için ortalama duyarlılık ve relaksometri değerleri hesaplanmış, ortalama, standart sapma, SEM ve voxel sayıları raporlanmıştır. Sonuç olarak, bu çalışma relaksometri ve QSM'yi bütünleştiren tekrarlanabilir bir preklinik qMRI çerçevesi ortaya koymakta; yöntemsel titizlik ve translasyonel potansiyel sergileyerek hastalık ve yaşlanma modellerinde mikroyapısal ve fizyolojik değişikliklerin incelenmesi için sağlam bir temel sunmaktadır.

Anahtar Sözcükler: Nicel MRG (qMRI), MRG, T_1 Haritalama, T_2 Haritalama, R_2^* Haritalama, Nicel Duyarlılık Haritalama (QSM), Wistar Sıçan, Preklinik, Beyin.

TABLE OF CONTENTS

LIST OF FIGURES

LIST OF TABLES

LIST OF SYMBOLS

M_z	Longitudinal Magnetization Vector
M_{xy}	Transverse Magnetization Vector
T_1	Longitudinal Relaxation Time
T_2	Transverse Relaxation Time
R_2^*	Transverse Relaxation Rate
χ	Susceptibility
ϕ	Unwrapped Phase
ψ	Wrapped Phase
∇^2	The Laplacian Operator

LIST OF ABBREVIATIONS

MRI	Magnetic Resonance Imaging
QSM	Quantitative Susceptibility Mapping
SWI	Susceptibility Weighted Imaging
STI	Susceptibility Tensor Imaging
qMRI	Quantitative MRI
DWI	Diffusion Weighted Imaging
DTI	Diffusion Tensor Imaging
T1w	T1 Weighted
T2w	T2 Weighted

1. INTRODUCTION

1.1 Magnetic Resonance Imaging

Magnetic resonance imaging (MRI) is an important modality helping medical staff and researchers explore the internal world of the human body. The first MR scanner was introduced in the 1980s, and now MRI is used in a myriad of ways to examine both the structure and function of various organs and systems in the body, and it is an essential tool used for diagnosis, prognosis, and treatment [5],[6]. MRI utilizes the magnetic properties of spins (including various atoms like Hydrogen, Sodium etc.) and quantum principles to localize structures and tissues based on their molecular content and spatial location in the body. The basis for MRI is magnetization of the nuclei, which are excited by turning RF coils on, then off, to detect the signal. These signals form the basis for reconstructing the image using various mathematical operations like the Fourier transform.

We first start by reviewing the distinction between qualitative and quantitative images in the next section. We then go on in Section 1.3 to review the principles of MRI, starting from simple spins and gradually advancing toward magnetization of volumes, and how these properties are used to acquire images. We then proceed in Sections 1.4 and 1.6 to review how these physical processes and properties give rise to quantitative images, and we demonstrate the various applications where this kind of images are used in both humans and animals in Section 1.7. The derivations used in the description of MRI principles are based on a few famous textbooks like **Principles of Magnetic Resonance Imaging: A Signal Processing Perspective [7]** and **Susceptibility Weighted Imaging in MRI: Basic Concepts and Clinical Applications [1].**

A description is then given of the work done as part of this thesis, covering subjects, data acquisition, data management, optimization, and data processing and analysis. The results are later discussed, and further work is suggested for the future.

Detailed derivations of key methods are provided in the Appendices.

1.2 Quantitative MRI

MRI serves as a camera that enables us to see inside the body non-invasively, and as with all cameras, images depend on a variety of factors like the scanner's strength, coils used, flip angle, and many more. It might be safe to say that it is similar to taking a photo of a tree with a camera. It is possible to change the settings of the camera like exposure, aperture, ISO, and shutter speed to give different pictures of the same tree. Taking the photo from a position closer to the tree will make the tree look larger, and taking it from far away will make it look smaller in the picture. But that does not mean it is shrinking or expanding. Similarly, the different parameters that we will explore (like the T_1 and T_2 relaxation times) provide contrast mechanisms, and they enable acquisition of images that show relative intensities of tissues in the brain depending on how we choose the imaging parameters. However, just like the tree, tissues have inherent physical properties, and just like the tree, it is possible to *measure* these physical properties. Images that show us relative intensity information are *qualitative*, whereas images that measure the inherent physical properties are *quantitative*.

Quantitative MRI (qMRI) is the subspecialty of MRI that is interested in this kind of measurements (other subspecialties include functional MRI and MR angiography). The first time this term was used was in a small meeting in 1997 at Dundee, Scotland, which was held by the UK Institute of Physics and Engineering in Medicine [8]. Although qMRI is more demanding, it provides advantages like increased reliability and reproducibility. Furthermore, developments in MRI technology, and efforts for international standardization make qMRI a burgeoning field that has a potential of massive contribution to our knowledge of both the structure and function of the human body, in health and disease.

1.3 Principles of MRI

1.3.1 Behavior of Spin Systems

Complex biological tissues consist of simpler substances that can be broken down into molecules, which in turn consist of atoms with nuclei and electrons. Nuclei have properties like the number of protons and neutrons (so-called mass number or atomic weight). Nuclei with odd atomic weights have an angular momentum ($\vec{J}$), also known as *spin* [7].

A volume in a magnetic field of an MR scanner can be considered a spin system to derive and understand its behavior. This system is linear and activated by an RF signal, which delivers energy when it is on. When the pulse is turned off, the system will go back to equilibrium as it emits the energy it absorbed in the form of a detectable signal. The basis of magnetic resonance imaging is the property of spin systems called *nuclear magnetism*, which is created when the system is placed in an external magnetic field like that of the MR scanner.

A moving electrical charge generates a magnetic field, thus a spinning proton induces a magnetic field in its vicinity because of the spinning motion. This magnetic field is denoted by $\vec{\mu}$ and called the *magnetic moment* or the *nuclear magnetic dipole moment*. In such a case, spin angular momentum is related to magnetic moment vectors as in $\vec{\mu} = \gamma\vec{J}$ where γ is called the *gyromagnetic ratio* and is a constant specific to each nucleus (for example, the gyromangetic ratio of Hydrogen is 42.58 MHz/T). According to quantum mechanics principles, the magnitude of this vector ($|\vec{\mu}|$ or μ for short) is described as $\mu = \gamma\hbar\sqrt{I(I+1)}$, where $\hbar = \frac{h}{2\pi}$ and h is Planck's constant, and I is the nuclear spin quantum number. I is related to atomic weights:

- If the number of protons and the number of neutrons are both even numbers, I is zero. When a nucleus has a nuclear spin quantum number of zero, it is not NMR-active. i.e., it does not react to being placed in a magnetic field.

- If the number of protons and the number of neutrons are both odd numbers, I is an integer.
- If the sum of the number of protons and the number of neutrons is odd, I is a half-integer, and the spin system is called a spin-$\frac{1}{2}$ system. An example of this is the proton (Hydrogen atom) with a spin quantum number of $\frac{1}{2}$.

When the spin system is not in a magnetic field, the spin vectors point in random directions, and a net magnetization vector does not exist. To generate magnetism from a spin system, the system needs to be placed in a magnetic field. Assuming the field is applied in direction of the positive z axis in the Cartesian coordinate system (this means that $\vec{B_0} = B_0\vec{k}$), the z-component of the spin system can have $2I+1$ orientations:

$$\mu_z = \gamma m_1 \hbar \mid m_1 = -I, -I+1, ..., I \tag{1.1}$$

The angle between $\vec{B_0}$ and $\vec{\mu}$ is

$$\cos\theta = \frac{\mu_z}{\mu} = \frac{m_1}{\sqrt{I(I+1)}} \tag{1.2}$$

μ also has a transverse component $\vec{\mu}_{xy}$ which is defined as $\vec{\mu}_{xy} = \mu_x\vec{i} + \mu_y\vec{j}$. It is possible to express the components as:

$$\begin{aligned} \mu_x &= |\vec{\mu}_{xy}| \cos\zeta \\ \mu_y &= |\vec{\mu}_{xy}| \sin\zeta \end{aligned} \tag{1.3}$$

Where ζ is a random variable with a uniform distribution over $[0, 2\pi)$. Thus, $|\vec{\mu}_{xy}| = \sqrt{\mu^2 - \mu_z^2} = \gamma\hbar\sqrt{I(I+1) - m_1^2}$.

So, for protons, since $I = \frac{1}{2}$ and $m_1 = -\frac{1}{2}, \frac{1}{2}$:

$$\begin{aligned} \cos\theta &= \pm\frac{1/2}{\sqrt{3/4}} \\ \Rightarrow \theta &= \pm 54^{\circ}44' \\ &\text{and} \\ |\vec{\mu}_{xy}| &= \frac{\gamma\hbar}{\sqrt{2}} \end{aligned} \tag{1.4}$$

This means they either align with or against the magnetic field's z-component (i.e. either parallel or anti-parallel). When a spin is placed in a magnetic field, it is known from classical mechanics that $\vec{\mu}$ experiences a torque from the external field, which can be described as the rate of change of its angular momentum:

$$\begin{aligned} \frac{d\vec{J}}{dt} &= \vec{\mu} \times B_0\vec{k} \\ \text{But since } \vec{\mu} = \gamma\vec{J}&\text{:} \\ \frac{d\vec{\mu}}{dt} &= \gamma\vec{\mu} \times B_0\vec{k} \end{aligned} \tag{1.5}$$

Since $\vec{\mu}$ has different components, it is possible to compute the cross product as:

$$\begin{aligned} \vec{\mu} \times B_0\vec{k} &= \begin{vmatrix} \vec{i} & \vec{j} & \vec{k} \\ \mu_x & \mu_y & \mu_z \\ 0 & 0 & B_0 \end{vmatrix} \\ &= \mu_y B_0\vec{i} - \mu_x B_0\vec{j} \\ \Rightarrow \frac{d\vec{\mu}}{dt} &= \gamma\mu_y B_0\vec{i} - \gamma\mu_x B_0\vec{j} \\ \Rightarrow < \frac{d\vec{\mu}_x}{dt}, \frac{d\vec{\mu}_y}{dt}, \frac{d\vec{\mu}_z}{dt} > &= < \gamma\mu_y B_0, -\gamma\mu_x B_0, 0 > \end{aligned} \tag{1.6}$$

Which means the z-component will not change with time, provided there is no other field than B_0. To solve the differential equations, the second-order derivative can be taken:

$$\begin{aligned} \frac{d^2\mu_x}{dt^2} &= \gamma B_0\frac{d\mu_y}{dt} = -(\gamma B_0)^2\mu_x \\ \frac{d^2\mu_y}{dt^2} &= -\gamma B_0\frac{d\mu_x}{dt} = -(\gamma B_0)^2\mu_y \end{aligned} \tag{1.7}$$

A general solution of the form Ae^{iw_0t} (assuming the initial phase is zero) exists such

that:

$$\begin{aligned} \mu_x &= Ae^{jw_0t} \\ \Rightarrow \frac{d\mu_x}{dt} &= Ajw_0e^{jw_0t} \\ \Rightarrow \frac{d^2\mu_x}{dt^2} &= A(jw_0)^2e^{jw_0t} = -(\gamma B_0)^2\mu_x \\ \Rightarrow w_0 &= \pm\gamma B_0 \ \text{ (Larmor frequency)} \\ \mu_x(0) &= Ae^0 = A \ \text{ (Initial condition)} \end{aligned} \tag{1.8}$$

Similarly for μ_y:

$$\begin{aligned} \mu_y &= Ce^{jw_0t} \\ \Rightarrow \frac{d\mu_y}{dt} &= Cjw_0e^{jw_0t} \\ \Rightarrow \frac{d^2\mu_y}{dt^2} &= C(jw_0)^2e^{jw_0t} = -(\gamma B_0)^2\mu_y \\ \Rightarrow w_0 &= \pm\gamma B_0 \ \text{ (Larmor frequency)} \\ \mu_y(0) &= Ce^0 = C \ \text{ (Initial condition)} \end{aligned} \tag{1.9}$$

Here emerges the relationship $w_0 = \gamma B_0$, which describes the angular frequency of precession, also known as Larmor frequency, in terms of the gyromagnetic ratio and the field strength. Since $\vec{\mu}_{xy} = \mu_x\vec{i}+\mu_y\vec{j}$. We choose the rotation direction as clockwise, so:

$$\vec{w} = -\gamma\vec{B}_0 = -w_0\vec{k} \tag{1.10}$$

And we can write the vector $\vec{\mu}_{xy}$ in the form of a complex variable (to make use of the Euler identity), so:

$$\vec{\mu}_{xy} = \mu_x\vec{i} + \mu_y\vec{j} \sim \mu_{xy} = \mu_x + j\mu_y \tag{1.11}$$

Since both μ_x and μ_y are proportional to e^{jw_0t}, we can write:

$$\mu_{xy}(t) = \mu_{xy}(0)e^{-i\gamma B_0t} \tag{1.12}$$

Euler's identity states that $e^{i\theta} = \cos\theta + i\sin\theta$. So:

$$e^{-i\gamma B_0 t} = \cos\gamma B_0 t - i\sin\gamma B_0 t \tag{1.13}$$

Since $\mu_{xy}(0) = \mu_x(0) + i\mu_y(0)$, then:

$$\begin{aligned}\mu_{xy}(t) = (\mu_x(0) + i\mu_y(0)) \times (\cos\gamma B_0 t - i\sin\gamma B_0 t) = \\ \mu_x(0)\cos\gamma B_0 t - i\mu_x(0)\sin\gamma B_0 t + i\mu_y(0)\cos\gamma B_0 t + \mu_y(0)\sin\gamma B_0 t\end{aligned} \tag{1.14}$$

Separating the real and imaginary parts:

$$\begin{aligned}\mu_x(t) &= \mu_x(0)\cos\gamma B_0 t + \mu_y(0)\sin\gamma B_0 t \\ \mu_y(t) &= -\mu_x(0)\sin\gamma B_0 t + \mu_y(0)\cos\gamma B_0 t\end{aligned} \tag{1.15}$$

So, the behavior of the transverse and z-components of the vector $\vec{\mu}$ is:

$$\begin{aligned}\mu_x(t) &= \mu_x(0)\cos w_0 t + \mu_y(0)\sin w_0 t \\ \mu_y(t) &= -\mu_x(0)\sin w_0 t + \mu_y(0)\cos w_0 t \\ \mu_z(t) &= \mu_z(0)\end{aligned} \tag{1.16}$$

And in exponential notation:

$$\begin{aligned}\mu_{xy}(t) &= \mu_{xy}(0)e^{-i\gamma B_0 t} \\ \mu_z(t) &= \mu_z(0)\end{aligned} \tag{1.17}$$

Which is the equation describing *nuclear precession* in the presence of an external field B_0. This can also be written in matrix form as a multiplication of a rotation matrix with the spin vector: $\boldsymbol{\mu}(t) = \boldsymbol{R_z}(w_0 t)\boldsymbol{\mu}(0)$ where:

$$\begin{bmatrix}\mu_x \\ \mu_y \\ \mu_z\end{bmatrix} = \begin{bmatrix}\cos wt & \sin wt & 0 \\ -\sin wt & \cos wt & 0 \\ 0 & 0 & 1\end{bmatrix}\begin{bmatrix}\mu_x(0) \\ \mu_y(0) \\ \mu_z(0)\end{bmatrix} \tag{1.18}$$

So, this represents the state of a given individual spin at a given time.

1.3.2 Bulk Magnetization

To go from the behavior of an individual spin to the collective behavior of the whole system, a macroscopic magnetization vector $\vec{M}$ is used:

$$\vec{M} = \sum_{n=1}^{N_s} \vec{\mu}_n \tag{1.19}$$

According to the quantum theory:

$$\begin{aligned} E &= -\vec{\mu}.\vec{B}_0 = -\mu_z B_0 = -\gamma\hbar m_1 B_0 \\ m_1 &= \frac{1}{2} \\ \Rightarrow E_\uparrow &= -\frac{1}{2}\gamma\hbar B_0 \quad \& \quad E_\downarrow = \frac{1}{2}\gamma\hbar B_0 \end{aligned} \tag{1.20}$$

This means that, when the B_0 is on, spins take on one of the two energy states. So, the energy difference is:

$$\Delta E = E_\downarrow - E_\uparrow = \gamma\hbar B_0 \tag{1.21}$$

The Boltzmann relationship indicates that:

$$\frac{N_\uparrow}{N_\downarrow} = e^{\left(\frac{\Delta E}{KT_s}\right)} \tag{1.22}$$

Where:

$$\begin{aligned} N_\uparrow &: \text{number of spins aligning upward} \\ N_\downarrow &: \text{number of spins aligning downward} \\ T_s &: \text{the spin system's absolute temperature} \\ K &: \text{Boltzmann constant } (1.38 \times 10^{-23} J/K) \end{aligned} \tag{1.23}$$

Practically, $\Delta E \ll KT_s$, so using Taylor series:

$$e^{\left(\frac{\Delta E}{KT_s}\right)} = \frac{N_\uparrow}{N_\downarrow} \approx 1 + \frac{\Delta E}{KT_s} \approx 1 + \frac{\gamma\hbar B_0}{KT_s} \Rightarrow N_\uparrow - N_\downarrow \approx N_\downarrow \frac{\gamma\hbar B_0}{KT_s} \tag{1.24}$$

When the exponent is zero, $N_\uparrow = N_\downarrow \;\; \& \;\; N_s = N_\uparrow + N_\downarrow \Rightarrow N_s = 2N_\downarrow$

$$N_\uparrow - N_\downarrow \approx N_s \frac{\gamma \hbar B_0}{2KT_s} \tag{1.25}$$

Which shows that there is a difference of a tiny proportion $\frac{\gamma \hbar B_0}{2KT_s}$ of spins in the lower-energy state, which causes a macroscopic magnetization represented by the vector $\vec{M}$. The resulting bulk magnetization vector is:

$$\vec{M} = M_x \vec{i} + M_y \vec{j} + M_z \vec{k} \tag{1.26}$$

But since the transverse components of all spins rotate randomly around the z-axis, they cancel out, and the x- and y- components of $\vec{M}$ become 0. Using Eq. 1.20, the following can be derived:

$$\vec{M} = \left(\sum_{n=1}^{N_\uparrow} \frac{1}{2} \gamma \hbar - \sum_{n=1}^{N_\downarrow} \frac{1}{2} \gamma \hbar \right) \vec{k} = \frac{1}{2} \left(N_\uparrow - N_\downarrow \right) \gamma \hbar \vec{k} \tag{1.27}$$

indicating that the bulk magnetization vector is in the same direction as the positive z-axis. Its magnitude is therefore:

$$M_z^0 = |\vec{M}| = \frac{\gamma^2 \hbar^2 B_0 N_s}{4KT_s} \tag{1.28}$$

Which is valid for a spin-$\frac{1}{2}$ system. For example, for a spin system consisting of protons:

$$\begin{aligned} \gamma &= 42.58 \times 10^6 Hz/T \\ h &= 6.6 \times 10^{-34} J - s \\ T_s &= 300K (\text{Room temperature}) \\ K &= 1.38 \times 10^{-23} J/K \\ B_0 &= 1T \end{aligned} \tag{1.29}$$

$$\Rightarrow \frac{N_\uparrow - N_\downarrow}{N_s} \approx \frac{42.58 \times 10^6 \times 6.6 \times 10^{-34}}{2 \times 1.38 \times 10^{-23} \times 300} \approx 3 \times 10^{-6}$$

Which means that 3 in each one million spins in a hydrogen spin system are activated when placed in a magnetic field.

1.3.3 RF Pulses

In order to give the magnetized spins energy and tip them away from the z-axis, another magnetic field is used to deliver an electromagnetic wave. This new magnetic field is therefore oscillatory (in the radio-frequency range) and is denoted $\vec{B}_1(t)$. To start with, according to the quantum model, the energy of an electromagnetic radiation of frequency w_{rf} is (according to Planck's law):

$$E_{rf} = \hbar w_{rf} \tag{1.30}$$

So, to change the energy state spins from one state to another, the energy of radiation should match the energy difference ΔE. So:

$$\hbar w_{rf} = \Delta E = \gamma \hbar B_0 \Rightarrow w_{rf} = w_0 \tag{1.31}$$

Which is the resonance condition, meaning that only when this happens, the spins change state. This amount of energy is delivered to the system using another field generated by the coils -the B_1 field.

A typical B_1 field is of the form [7]:

$$\vec{B}_1(t) = 2B_1^e(t)\cos(w_{rf}t + \phi)\vec{i} \tag{1.32}$$

where

$$\begin{aligned} B_1^e(t) &: \text{pulse envelope function} \\ w_{rf} &: \text{frequency of excitation pulse} \\ \phi &: \text{initial phase} \end{aligned} \tag{1.33}$$

The field is *linearly polarized* for the fact that it oscillates linearly along the x-axis. This can be separated into two fields oscillating circularly in opposite directions:

$$\begin{aligned} \vec{B}_1(t) = B_1^e(t)[\cos(w_{rf}t + \phi)\vec{i} - \sin(w_{rf}t + \phi)\vec{j}] \\ + B_1^e(t)[\cos(w_{rf}t + \phi)\vec{i} + \sin(w_{rf}t + \phi)\vec{j}] \end{aligned} \tag{1.34}$$

and the first term rotates clockwise, whereas the second rotates counterclockwise. So, in the case of oscillating in the resonance frequency, the second component exerts a negligible effect and it is possible to neglect it. Considering the part contributing to resonance, it has two components:

$$\begin{aligned} B^e_{1,x}(t) &= \cos(w_{rf}t + \phi)\vec{i} \\ B^e_{1,y}(t) &= -\sin(w_{rf}t + \phi)\vec{j} \\ \Rightarrow B_1(t) &= B^e_{1,x}(t) + jB^e_{1,y}(t) = B^e_1(t)e^{-j(w_{rf}t+\phi)} \end{aligned} \tag{1.35}$$

The main properties that characterize a B_1 field are the envelope function B^e_1, the carrier frequency w_{rf}, and the initial phase ϕ. Widely used B^e_1 functions include the rectangular and the Sinc pulses.

$$B^e_1(t) = B_1\Pi\left(\frac{t - \tau_p/2}{\tau_p}\right) = \begin{cases} B_1 & 0 \leqslant t \leqslant \tau_p \\ 0 & \text{Otherwise} \end{cases} \tag{1.36}$$

$$B^e_1(t) = \begin{cases} B_1 sinc(\pi f_w(t - \tau_p/2)) & 0 \leqslant t \leqslant \tau_p \\ 0 & \text{Otherwise} \end{cases} \tag{1.37}$$

1.3.4 The Bloch Equation

The Swiss-American physicist Felix Bloch described the phenomenon of nuclear induction in 1946 [9] and later received the Nobel prize in physics in 1952 with Edward Mills Purcell for their contributions to nuclear magnetic precision measurement [10]. As shown previously in Eq. 1.5, the magnetization vector behavior with time can be described by:

$$\frac{d\vec{M}}{dt} = \gamma\vec{M} \times \vec{B} \tag{1.38}$$

But assumes that magnetization vector is only affected by an external field. However, there are other forces in action that affect this behavior including thermal agitation and interaction between neighboring nuclei [9]. To account for these effects, the mag-

netization vector should be examined separately for both factors.

A very fundamental difference between the two is that while thermal agitation introduces energy to the system, interaction between the nuclei does not. As can be seen and previously stated in Eq. 1.20:

$$E = -\mu_z B_0 \tag{1.39}$$

This means that energy changes are caused by changes in the longitudinal component (z-component) of the magnetization vector, and it is thermal perturbations that are responsible for these changes. Let the equilibrium value of the longitudinal component of the magnetization vector be M_0. If it is ever the case that $M_z \neq M_0$, it will try to go back to this value in an exponential manner, and the process is characterized by the time constant T_1 which, as coined in the original paper, is called the "thermal" or "longitudinal" relaxation time. It is thus possible to describe the rate of change of M_z caused by thermal perturbations only using the differential equation:

$$\frac{dM_z}{dt} = -\frac{M_z - M_0}{T_1} \tag{1.40}$$

Due to thermal agitation of the surrounding nuclei as well, their fields contribute to the establishment of equilibrium. Normally they are too small and can make the thermal relaxation time very long, and their effect on T_1 is negligible. But these interactions are important for the changes of the transverse components M_x and M_y. The change of these components is assumed to be exponential just like the longitudinal component. So, it is possible to describe their behavior by the equations:

$$\begin{aligned} \frac{dM_x}{dt} &= -\left(\frac{1}{T_2}\right) M_x \\ \frac{dM_y}{dt} &= -\left(\frac{1}{T_2}\right) M_y \end{aligned} \tag{1.41}$$

Then the overall rate of change of $\vec{M}$ can be obtained by adding Eq. 1.38, Eq. 1.40,

and Eq. 1.41. So:

$$\frac{d\vec{M}}{dt} = \gamma\vec{M} \times \vec{B} - \frac{M_x\vec{i} + M_y\vec{j}}{T_2} - \frac{(M_z - M_0)\vec{k}}{T_1} \tag{1.42}$$

Where M_0 is, as stated previously, the equilibrium value for $\vec{M}$ in the presence of $\vec{B}_0$ only. The last two terms can be dropped to examine the behavior of the magnetization vector in the presence of $\vec{B}_0$ under the radio frequency excitation period. This is permissible if the RF pulse is transitory in comparison to T_1 and T_2, which is practically the case.

1.3.5 Echoes

Following excitation of the spins using an RF pulse, and after the pulse is turned off, spins start going back to equilibrium (Eq. 1.42 describes this process and it is explored in detail in Section 1.4). As the spins go to equilibrium, the change in magnetic flux through detection coils generate a signal according to Faraday's law. The simplest form of this signal is Free Induction Decay.

1.3.5.1 Free Induction Decays. A free induction decay (FID) is produced by the action of a single pulse on a nuclear spin system. The FID signal represents the most fundamental type of a transient response following pulse excitation and serves as the parent signal from which other MR signal forms, discussed later in this section, are derived. Mathematically, the FID signal generated by an α pulse can be expressed as

$$S(t) = \sin\alpha \int_{-\infty}^{\infty} \rho(w) e^{-t/T_2(w)} e^{-iwt} dw \qquad t \geq 0 \tag{1.43}$$

Two properties of an FID signal are the amplitude and the rate of decay. The maximum amplitude occurs at $t = 0$ whose value is

$$\sin\alpha \int_{-\infty}^{\infty} \rho(w) dw = M_z^0 \sin\alpha \tag{1.44}$$

The decay rate of an FID signal is strongly tied to the underlying spectral distribution. Therefore, an FID signal is the transient response of a spin system following pulse excitation. The signal's magnitude depends on the flip angle, the total number of spins, and the strength of the magnetic field. How long the signal lasts depends to a large extent on how inhomogeneous the field is, which is described by the T_2^* decay.

1.3.5.2 RF Echoes. Another form of MR signal is the so-called *echo*. Visually, an echo signal appears as two consecutive FID signals in opposite directions (the first from refocusing and the second from the dephasing of the transverse magnetization) [7]. Echoes can be generated using RF pulses (spin-echoes), or magnetic gradients (discussed next in Section 1.3.5.3). The essential requirement for generating a spin-echo is two consecutive pulses, the first one is for exciting the spins, after which the spins start dephasing, then the second pulse changes the direction of spinning so that the spins rephase and generate an echo. This is denoted as

$$90^\circ - \tau - 180^\circ$$

where the 90° pulse excites the spins, and the 180° pulse rephases them. The echo is detected at 2τ where τ is a time delay after the 90° pulse. The echo signal form can be generalized for arbitrary excitation and refocusing angels, and it could be extended for a larger number of pulses. Bloch equations can be used to analyze echoes but it can get complicated for larger numbers of echoes, so Carr-Purcell-Meiboom-Gill (CPMG) echo trains are used to simplify analysis of consecutive echoes. Each side of an echo (after the first excitation or refocusing pulse) decays in a T_2^* relaxation, and the amplitude of the spin echo decays in a T_2-weighted relaxation.

1.3.5.3 Gradient Echoes. This kind of echoes are generated using time dependent gradient magnetic fields. The key concept is that a gradient field can deliberately dephase and rephase a signal to generate one or more echo signals. In this context, a gradient field is a type of inhomogeneous field whose z-component varies linearly along a specific direction, referred to as the gradient direction. So, a gradient field $\vec{B}_G$ is a

y-gradient field if $B_{G,z} = G_y y$ or a z-gradient field is $B_{G,z} = G_z z$

The gradient system in MR scanners consists of three gradient coils: the x-, y-, and z-gradient coils. Each of them produce a gradient field along its axis. Although all the fields have components in the x- and y-axes, they are ignored because the B_0 field is so strong in the z-direction. So, $B_{G,z}$ is often loosely referred to as the gradient field, and $B_{G,z}$ and B_G may be used synonymously. So, the net magnetic field when a gradient field is active in the region of interest can be described as

$$B_{G,z} = G_x x + G_y y + G_z z \quad \Rightarrow \vec{B} = (B_0 + G_x x + G_y y + G_z z)\vec{k} \tag{1.45}$$

if the three gradient coils are used simultaneously. The three gradients can be represented in a single gradient vector

$$\vec{G} = (G_x, G_y, G_z) = G_x\vec{i} + G_y\vec{j} + G_z\vec{k} \tag{1.46}$$

where the direction of $\vec{G}$ represents the gradient direction of $\vec{B}_G$ or $\vec{B}$. $\vec{G}$ is also a function of time, if $\vec{G}$ is a constant in the time interval of interest, the gradient field is called a static field. Otherwise, the field is a time-varying gradient field. Both are used in various MRI applications. The relevant aspect of gradient fields is their impact on phase.

By definition, phase is the time integral of frequency. In a spin system, the frequency is $w = \gamma B$ and the phase is thus

$$\phi(\vec{r}, t) = \int_0^t w(\vec{r}, \tau)d\tau = \gamma \int_0^t B(\vec{r}, \tau)d\tau \tag{1.47}$$

For example, in a linear gradient field $\vec{G}(t)$, the magnetic field becomes $B(\vec{r}, t) = B_0 + \vec{G}(t)\vec{r}$. In the rotating frame, B_0 disappears, and the phase can be described as

$$\gamma\vec{r}\int_0^t \vec{G}(\tau)d\tau \tag{1.48}$$

For simplicity, the case following the deliverance of an α-degree RF pulse is considered, where a positive gradient in the x-direction is used so that spins in different x-locations

will have different phase values [1]. This can be described in the rotating frame as

$$\phi(x,t) = \gamma \int_0^t -G_x x dt' = -\gamma G_x x t \quad | \quad 0 \leq t \leq \tau \tag{1.49}$$

1.4 Relaxometry

As explored so far, after exciting the spins with a short lasting RF pulse, spins start a process of relaxation in which they return to the equilibrium state, while producing a detectable signal. Eq. 1.42 describes the overall process. However, the first term can be dropped while examining the process of relaxation itself (i.e. after the RF pulse is off). So, the following two components describe the process of relaxation:

$$\begin{aligned} \frac{dM_z}{dt} &= -\frac{M_z - M_0}{T_1} \\ \frac{dM_x}{dt} &= -\left(\frac{1}{T_2}\right) M_x \\ \frac{dM_y}{dt} &= -\left(\frac{1}{T_2}\right) M_y \end{aligned} \tag{1.50}$$

It is possible to combine the x and y components to represent the transverse relaxation component, which is characterized by the T_2 time constant. Thus yielding:

$$\begin{aligned} \frac{dM_z}{dt} &= -\frac{M_z - M_0}{T_1} \\ \frac{dM_{xy}}{dt} &= -\left(\frac{1}{T_2}\right) M_{xy} \end{aligned} \tag{1.51}$$

which are separable ordinary differential equations. Each component is examined separately.

1.4.1 T_1 Relaxation

To solve

$$\frac{dM_z}{dt} = -\frac{M_z - M_0}{T_1} \tag{1.52}$$

we start by rearranging the equation as

$$\frac{dM_z}{M_z - M_0} = -\frac{dt}{T_1} \tag{1.53}$$

and it becomes possible to integrate both sides:

$$\begin{aligned} \int \frac{dM_z}{M_z - M_0} &= \int -\frac{dt}{T_1} \\ \ln|M_z - M_0| &= -\frac{t}{T_1} + C \\ M_z - M_0 &= C' e^{\frac{-t}{T_1}} \end{aligned} \tag{1.54}$$

at t = 0:

$$M_z(0) - M_0 = C' e^0 \Rightarrow C' = M_z(0) - M_0$$

$$\Rightarrow \boxed{M_z(t) = M_0 + (M_z(0) - M_0)\, e^{-t/T_1}}$$

1.4.2 T_2 Relaxation

To solve

$$\frac{dM_{xy}}{dt} = -\left(\frac{1}{T_2}\right) M_{xy} \tag{1.55}$$

we start by rearranging the equation as well, it becomes

$$\frac{dM_{xy}}{M_{xy}} = -\frac{dt}{T_2} \tag{1.56}$$

and we then integrate both sides:

$$\begin{aligned} \int \frac{dM_{xy}}{M_{xy}} &= -\int \frac{dt}{T_2} \\ \ln|M_{xy}| &= -\frac{t}{T_2} + C \\ M_{xy}(t) &= C' e^{-t/T_2} \end{aligned} \tag{1.57}$$

at t=0:

$$M_{xy}(0) = C' e^0 \Rightarrow C' = M_{xy}(0)$$

$$\Rightarrow \boxed{M_{xy}(t) = M_{xy}(0) e^{-t/T_2}}$$

1.4.3 T_2^* Relaxation and R_2^*

Usually, spin-echo is used for getting T_1 and T_2 images. While, in contrast, gradient echo (Section 1.3.5.3) is used, the spins are more prone to field inhomogeneities and interactions between each other, and the transverse relaxation disappears more quickly, giving rise to the T_2^* relaxation time. So the signal model is the same as that of T_2, but the sequence used for producing the images is different. T_2 and T_2^* are related by

$$\begin{aligned} \frac{1}{T_2^*} &= \frac{1}{T_2'} + \frac{1}{T_2} \\ R_2^* &= R_2' + R_2 \end{aligned} \tag{1.58}$$

Where R_2^* is defined as the relaxation rate, and is the reciprocal of T_2^* as can be seen in the equation.

1.4.4 Mapping of Relaxation Times and Rates

The discussion thus far of the diverse relaxation parameters have been about understanding their physical basis using what is known about the spin system and its dynamics. Eq. 1.54 and 1.57 describe how the longitudinal and transverse magnetization vectors, respectively, behave in the real world, and Eq. 1.58 defines how that behavior changes when field inhomogeneities are more prominent.

To observe this behavior, record it, and make it into data, proper use of echoes (Section 1.3.5) is needed so as to acquire signals at proper time points that enable observation of the process of relaxation at the time of acquisition. In other words, sequences are used to create echos at different points, so as to sample the relaxation process. This is followed by preprocessing that uses the acquired raw signals to find the relaxation time/rate parameters for each voxel according to that voxel's relaxation pattern. This process of defining proper models, fitting them, and computing quantitative relaxometry (T_1, T_2, and R_2^*) maps is called **mapping (T_1 mapping generates**

T_1 maps, T_2 mapping generates T_2 maps, and so on).

Proper models can be different for the same parameter depending on the sequence used to acquire the images. For example, spin-echo based sequences are generally used for acquiring T_1 and T_2 images at different times. That data is then used to construct timeseries for each voxel, and fit the constructed signal to a signal model, to get a quantitative map. One of the sequences used for T_1 mapping is the inversion recovery (IR) which uses the signal model

$$S(TI) = A - Be^{-TI/T_1} \tag{1.59}$$

where continuous time (t) in Eq. 1.54 is replaced by inversion time (TI), which is the time point at which the images are acquired. But other models exist for T_1 fitting for different sequences like the variable flip angle (VFA), or the Look-Locker technique where the signal model is

$$e^{-TR/T_1^*} = \cos(\alpha)e^{-TR/T1} \tag{1.60}$$

where α is a small flip angle used for exciting the spins, and TR is time of repetition [8]. Description of the mapping options used in this work is described in detail in Section 2.4.

1.5 Relationship of Phase and Magnetic Susceptibility

Electrons around the spins form another source of inhomogeneity in the form of so-called shielding effect, as these charges have their own magnetic properties that affect those of the nuclei. This is all related to the concept of susceptibility which is defined as the extent to which a material is affected when it is exposed to a magnetic field. Physically, susceptibility $(\chi) = \frac{M}{H}$, where M is the ratio of magnetization within the material, and H is the strength of the applied magnetic field. Materials can be paramagnetic ($0 < \chi < \epsilon | \epsilon$: a small positive number), ferromagnetic ($1 << \chi$), and diamagnetic ($-1 < \chi < 0$) [1]. Paramagnetic materials (like deoxyhemoglobin) are

weakly attracted when in a magnetic field, and this property of deoxyhemoglobin is utilized in fMRI to observe blood flow and assess brain activity accordingly. Diamagnetic materials are weakly repelled when in a magnetic field, whereas ferromagnetic materials are strongly attracted when in a magnetic field, and they are the most encountered magnetic materials in daily life. The behavior of these materials in the presence of an external magnetic field disturbs the magnetic field around them, causing an inhomogeneity. This inhomogeneity in the magnetic field causes a difference in the precession frequency, and therefore in the phase (as time passes). This means that it is possible -as will be shown- to use phase information to obtain further insight into susceptibility. However, before going into how to do so, it should be noted how phase can be obtained and used.

As shown in Section 1.3.5.3, phase accumulates as time (Time to Echo or TE in this case) passes, and that relationship is described in Eq. 1.49 [8],[1]. Multi-echo gradient echo images are preferred to take advantage of the contrast enhancement with time, and it is possible to acquire phase images as well as magnitude images of the same gradient echo scan. Phase information is used consequently to obtain susceptibility-related images, which include susceptibility weighted imaging (SWI), susceptibility tensor imaging (STI), and quantitative susceptibility mapping (QSM) [4]. Susceptibility weighted imaging utilizes the relationship between susceptibility and phase in that after getting phase values due to local susceptibility of tissues, masking is used to stress phase values of interest. For example, if negative phase is of interest, a mask is constructed such that negative phase values are kept, and it is consecutively multiplied multiple times with the magnitude image to stress positions of negative phase, thus emphasizing them and increasing contrast [1]. QSM goes one step further and tries to map the quantitative susceptibility of the underlying tissue by solving the so-called inverse problem, where local phase shifts are used to map susceptibility using a dipole kernel. However, to do so, the dipole kernel is assumed to be isotropic, which has been found not to be the case in regions like white matter where the microstructure of the tissue makes susceptibility anisotropic [11]. STI obviates the need for this assumption by using multiple angles to measure phase by changing the orientation of the imaged volume inside the scanner. The different orientations are then analyzed together to

yield the susceptibility tensor [1].

1.6 Quantitative Susceptibility Mapping

Sources of susceptibility include iron deposition and myeline to count a few. These cause structural changes in the brain, and are associated with aging, neurodegenerative diseases [12],[13], and psychiatric disorders [14],[15],[16],[17],[18] (applications are further explored in Section 1.7). Therefore, it is possible to use this quantitative information to derive biomarkers for different conditions. However, to obtain quantitative susceptibility information from phase images, some preprocessing of the raw phase images is necessary.

1.6.1 Phase Unwrapping

Phase images are reconstructed from raw, complex signals coming from the MRI scanner. To acquire phase from the complex signal, the trigonometric function atan2() (a two-argument version of the arctan function that takes the y and x components separately, instead of a single ratio, and uses the signs to determine the correct quadrant of the ray) is used. But the range of this function is $(-\pi, \pi]$. Thus, any phase value beyond this range is "wrapped" to its beginning $(-\pi)$. This introduces discontinuities in the phase image that need to be eliminated. An example of 1 dimensional phase wrapping is shown in Figure 1.1.

Various methods have been explored for phase unwrapping for both spatial and temporal domains, including path-based and linear fitting methods [4]. For example, the relationship between wrapped and unwrapped phase ($\phi = \psi + 2\pi k \,|\, k \in \mathbb{Z}$ where ϕ and ψ are unwrapped and wrapped phase, respectively) can be used with the Laplacian operator to retrieve the true phase value using the following relationship:

$$\phi \approx \frac{\nabla^2 \sin(\psi)\cos(\psi) - \nabla^2 \cos(\psi)\sin(\psi)}{\nabla^2} \tag{1.61}$$

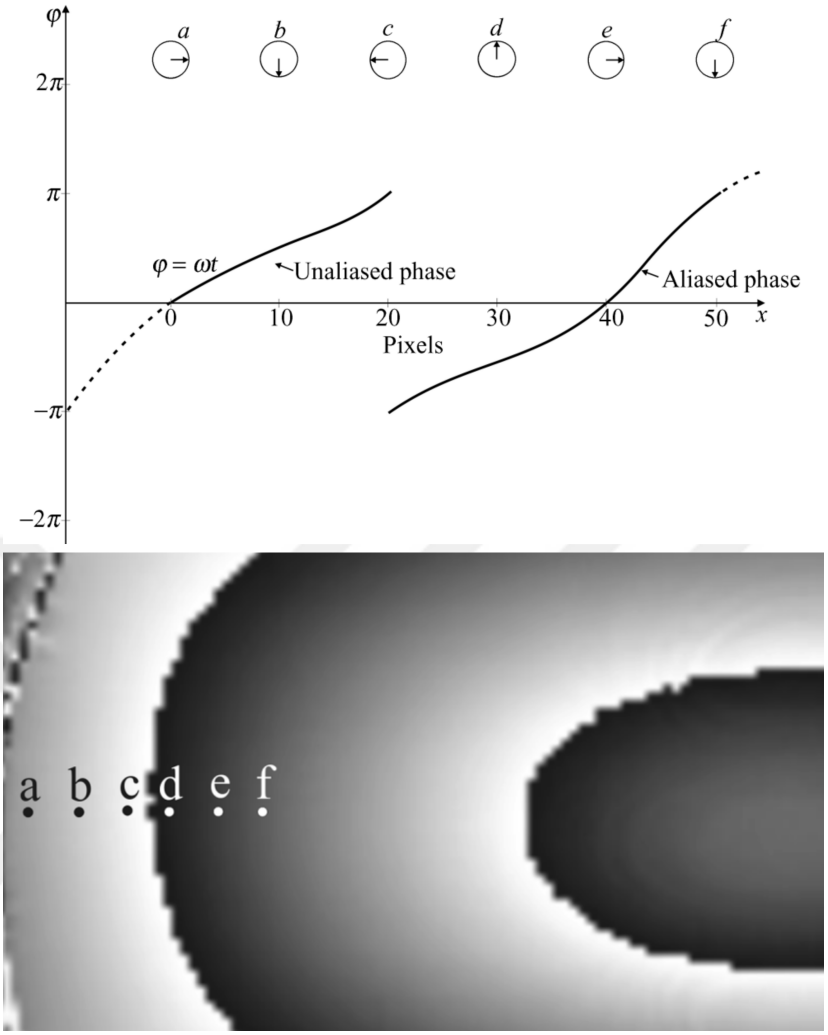

Figure 1.1 A depiction of 1D aliasing in phase images (phase wraps). Figures are taken from [1].

where ∇^2 is the Laplacian operator. Detailed derivation of this relationship can be found in Appendix A. Phase unwrapping gets rid of the discontinuities, as can be seen in Figure 1.2

1.6.2 Background Phase Removal

Unwrapping the phase produces the image of the total field. It is called the total field because it contains phase shifts due to tissue susceptibility differences, as well as phase shifts due to the "background" field. These shifts are mainly caused by large difference in susceptibility in air-tissue interfaces, as well as other sources outside

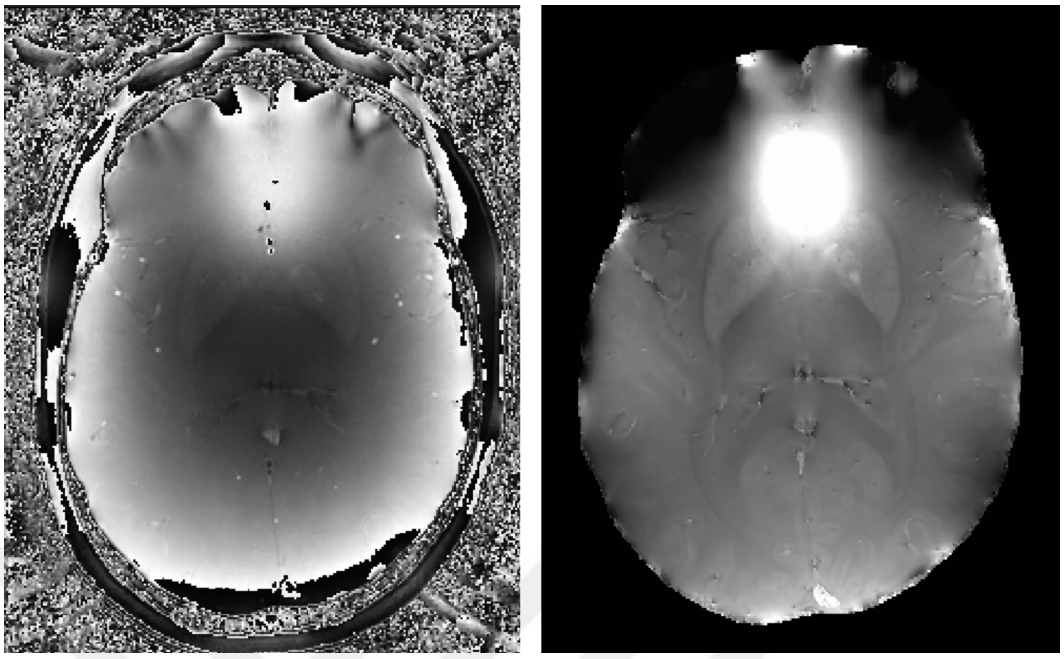

Figure 1.2 Phase unwrapping using the Laplacian operator removes the discontinuities in the raw phase image (left) and produces a total field image (right). Figures are created using the dataset provided by [2].

the body. Many methods exist for background field removal including Projection onto Dipole Field (PDF) [19], and Sophisticated Harmonic Artifact Reduction for Phase (SHARP) [20], as well as deep learning [21], and it is an active research area. A developed version of SHARP, namely v-SHARP (variable kernel size SHARP) is used in this work. But to understand it, SHARP should be introduced first.

As stated earlier, the total field is the sum of an internal field, which is the result of tissue susceptibility within the brain, and a background field due to air-tissue interface and other sources of susceptibility outside the brain, and both fields extend beyond their boundaries. However, susceptibility within the brain is orders of magnitude smaller than the main field, and the background field extends through all of the volume of interest (brain) and is harmonic. Using the spherical mean value property of harmonic functions, SHARP removes the background field by estimating the background field using a non-negative, radially symmetrical, normalized kernel (sphere). Detailed derivation of SHARP can be found in Appendix B.

As can also be seen in the derivation, SHARP uses the brain mask in the process

of removing the background field, so the result can vary depending on the choice of the brain mask. It also erodes the mask to avoid edge-related artifacts, and the amount of erosion depends on the size of the kernel. The erosion size should be enough to not allow any incorrect values from outside the brain to affect the field inside the brain. To reduce the effect of convolution toward the edge, a variable kernel size can be used where the radius of the spherical kernel depends on how far it is from the edge of the brain mask, which is the reasoning behind v-SHARP [22]. Figure 1.3 shows the result of background field removal. This represents the internal field B_{int} that is the result of the susceptibility distribution of the underlying tissue.

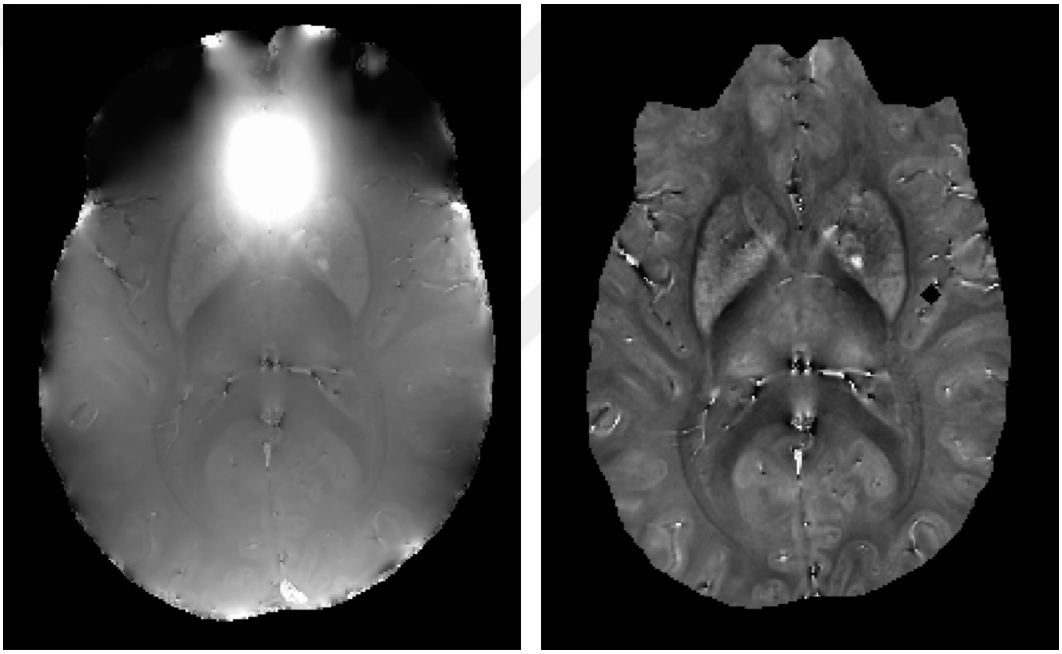

Figure 1.3 Background field is removed from the total field image (left) to yield the internal field (right). Figures are created using the dataset provided by [2].

1.6.3 Dipole Inversion

After removing the background field, we are left with the internal field, which can be shown to be

$$\Delta\omega = -\gamma B_0 \left(\chi(\vec{r}) \otimes d(\vec{r})\right) \tag{1.62}$$

where $\chi(\vec{r})$ is the susceptibility at position $\vec{r}$, d is the magnetic dipole, and $\otimes$ is the convolution operator. This is equivalent to

$$\Delta B = B_0 \left(\chi(\vec{r}) \otimes d(\vec{r})\right) \tag{1.63}$$

and the dipole kernel is calculated in k-space as

$$D(\boldsymbol{k}) = \frac{1}{3} - \frac{k_z^2}{k_x^2 + k_y^2 + k_z^2} \tag{1.64}$$

Figure 1.4 shows a depiction of the dipole kernel in the spatial domain as well as in the k-space.

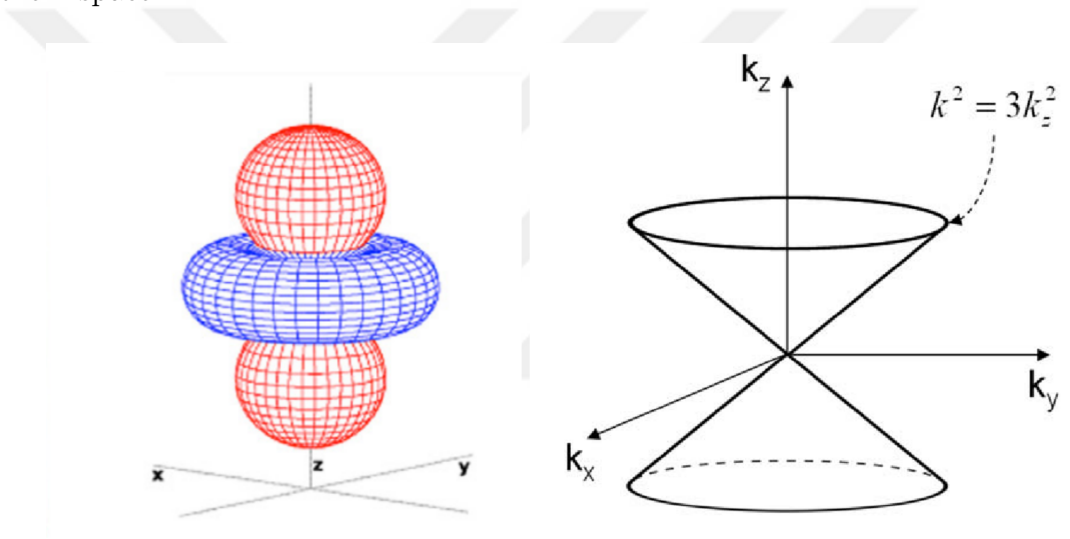

Figure 1.4 The magnetic dipole in the spatial domain (left) and its magnitude in k-space (right). Figures are taken from [3] and [4], respectively. The cone of zero is shown with arrows on the right.

It is then possible to compute the susceptibility distribution using deconvolution of the internal field with the dipole kernel. However, deconvolution corresponds to division in the Fourier domain, and the dipole kernel causes issues in division because of the so-called "cone of zero," which is the name given to regions where Eq. 1.64 equals zero (highlighted with arrows in Figure 1.4).

To overcome this, threshold-based k-space division (TKD) [23] sets a threshold for the kernel's values, so that all values below the threshold are made equal to it in k-space, thus preventing division by zero. This means that a threshold ε is chosen such

that:

$$\tilde{\chi}(\boldsymbol{k}) \;=\; \begin{cases} \dfrac{\Delta\tilde{B}_z(\boldsymbol{k})}{D(\boldsymbol{k})}, & |D(\boldsymbol{k})| \geq \varepsilon, \\ \dfrac{\Delta\tilde{B}_z(\boldsymbol{k})}{\varepsilon}, & |D(\boldsymbol{k})| < \varepsilon. \end{cases} \tag{1.65}$$

where the tilde (˜) indicates the Fourier space representation. A typical example of ε is 0.15.

One disadvantage of TKD is that it exacerbates noise and causes streaking artifacts, because of the hard cutoff threshold it applies all over the image. So, instead of just dismissing the regions on/close to the cone by thresholding them, a more sophisticated approach was explored that uses LSQR [24]. LSQR is an "algorithm for sparse linear equations and sparse least squares" that was formalized back in 1982 [25]. iLSQR uses the values below the threshold instead of setting all of them to a constant value, and it does so as follows.

Although the "zero cone" has a value of zero at the cone, the derivative of the kernel can provide useful information. So, the first-order derivative with respect to k_z is taken. This leads in few steps to an equation where susceptibility can be better estimated on/near the cone. So instead of dismissing all the data below a threshold, that data is used, and a piecewise function can be defined where in the regions away from the cone, it is the same deconvolution, but in the regions on/close to the cone, a computation is possible using the derivative. However, the derivation assumes phase values exist everywhere within the field of view (FoV), which is not the case. Phase values are only available within the brain, not outside it (this was also an important point in SHARP, which made erosion necessary). Therefore, masking is required in the spatial domain, which corresponds to convolution in the k-space (convolution of the Fourier representation of the multiplied mask and that of the actual local phase image), which modifies the actual k values in each voxel, rendering accurate calculation impossible. To overcome this, LSQR is used to iteratively solve the problem. Detailed derivation is in Appendix C.1. Figure 1.5 shows the result of dipole inversion (method used is unknown, figure used for illustration).

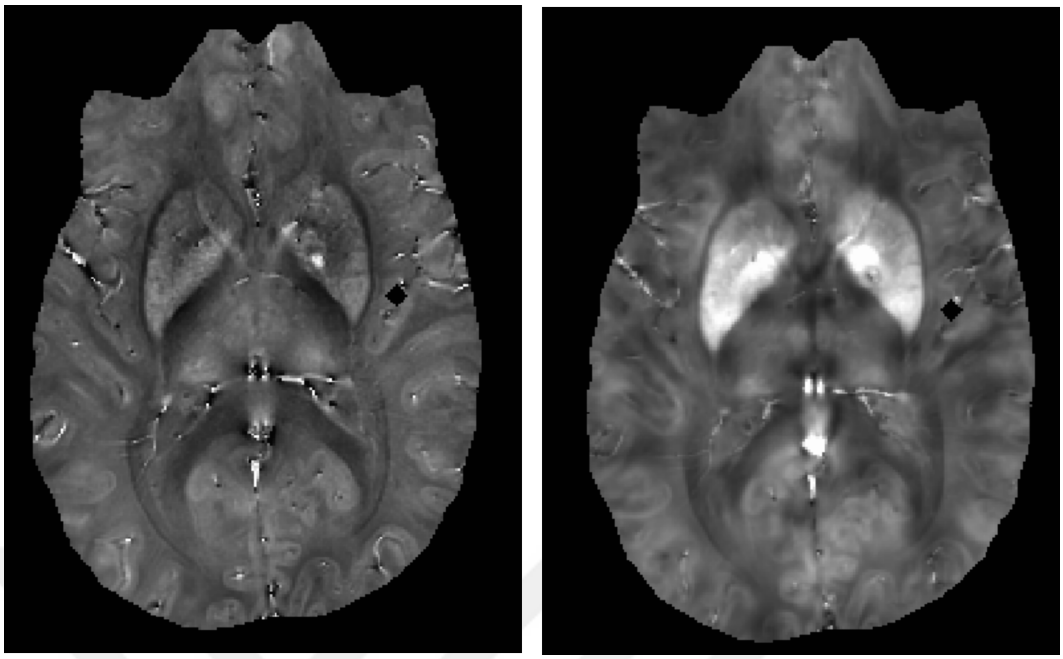

Figure 1.5 Internal field (left) is deconvolved with the dipole kernel, producing the quantitative susceptibility map (right - display range [-0.2 0.2] ppm). Figures are created using the dataset provided by [2].

Even with iLSQR, some images with a high dynamic range still show streaking artifacts in the end susceptibility map because of strong field sources. One suggested approach to overcome this is to use L1 and L2 regularization to first calculate susceptibility of strong field sources, then calculate the dipole field due to these strong sources and remove it from the total field, and finally use the remaining field to estimate susceptibility of weak sources to combine the two resultant maps at the end. This approach was found to lead to more streaking artifact reduction in QSM, and hence got its name (STAR-QSM) [26]. Finally, it should also be noted that various deep learning models have also been explored for this step. For example, a recent UNet based physics-informed deep learning model attempted reconstruction of QSM using local field images without the common assumption in classical algorithms that susceptibility is isotropic [27].

1.7 Literature on Applications of qMRI

Structural changes are observed in the aging rat brain [28],[29], which are also accompanied by functional changes [30]. These changing properties of the underlying brain tissue impact the quantitative parameters for that tissue. For example, T_1, T_2, and susceptibility are related to properties like water content, myelination, iron levels, and tissue structure. While a higher water content increases T_1 and T_2, myelination and elevated iron levels cause their decay [31],[32],[33],[34],[35]. This can be used in various application to better understand the changes taking place in the brain tissue. For example, T_1 values are shown in some studies to decrease with age [31],[32], and in others to increase [33],[35]. T_2 values have also been shown to change with age [34],[31].

In humans, T_2' values showed a strong negative correlation with age, suggesting elevated iron levels. T_2 values, on the other hand, increased with age, likely due to demyelination [31]. In another study, T_2 values in adolescents (17.4 ± 4.9 years) were found to vary in different ways depending on the region. For example, regions of the thalamus, putamen, globus pallidus, and others showed a decreased T_2 value, whereas in some cerebellar regions, T_2 is shown to be higher [34]. Iron levels have been shown to increase in the older group (12 subjects, female:male ratio 6:6, age: 74.4 ± 7.6 years) when compared to a younger group (11 subjects, female:male ratio 6:5, age: 24.0 ± 2.5 years) using QSM, especially in striatal and brain stem regions that include globus pallidus, substantia niagra, and putamen [36]. R_2^* was also used together with QSM in another study, with a higher number of subjects (40 subjects, 20 in each group, female:male ratio 11:9 in each group). Similarly, susceptibility increased in the older group (70 ± 1 years) compared to the younger one (24 ± 2 years), particularly in deep brain nuclei, putamen, thalamus, etc. However, a difference in the behavior of QSM and R_2^* in some regions could not be explained [37]. In another study where metabolites were also analyzed using spectroscopy as well as multiparametric qMRI, multiple ROIs showed altered metabolic content which is also correlated with changes in the T_1 and T_2 relaxation times. For example, in some ROIs, the longitudinal relaxation time was positively correlated with the increased concentration of metabolites like myo-inositol (mI), total creatine and phosphocreatine (tCr), and glutamine and glutamate (Glx)

[38].

qMRI can also be used in psychiatry. For example, in a study, 231 children (121 ADHD group, age: 8.44 ± 2.13 years; 110 control group, age: 8.56 ± 2.54 years) were prospectively chosen, and QSM was used to investigate brain iron level, which was found to be lower in regions like the globus pallidus, caudate nucleus, frontal lobe, putamen, and hippocampus in the ADHD group compared to the control group [18]. Likewise, children of age 3-6 (study group included 40 subjects aged 2-6 years) who were diagnosed with Autism had lower susceptibility values in regions like the frontal white matter, caudate nucleus, substantia nigra, dentate nucleus, and the red nucleus compared to the control group (40 subjects aged 2-6 years) [17]. Another study found significant increases in susceptibility in brain regions that include frontal and temporal lobe structures, putamen, thalamus, and cerebellum in patients (sample size: 21) with recurrent depression compared to the control group (sample size: 20) [14]. QSM was also used for studying psychosis, where a group of patients (83 subjects, mean age 20 years) was compared to a control group (64 subjects, mean age 23). Susceptibility was found to be significantly lower in the patients group in the putamen and globus pallidus [15].

In rats, T_2 mapping was used to study the effect of exposure to organophosphate toxicant (prevalent in pesticides). 49 male Sprague Dawley rats were randomly divided into a control group and an intoxicated group. The intoxicated group was then randomly divided into 3 groups that received different treatment protocols. Subjects were then scanned on the 3^{rd}, 7^{th}, and 28^{th} days after exposure. Intoxicated subject had higher T_2 values in all regions compared to the control group, and they decreased with time. A combination of two drugs for treatment proved better, which was reflected in T_2, thus suggesting T_2 as a possible indicator to evaluate injury and treatment [39]. QSM, T_1 mapping, and diffusion were also used to study a mice model of amyloid pathology [40]. T_1 and T_2 were also used for studying the effect of different antidepressants in rat models of depression, and behavioral changes were consistent with the change in these values [41]. T_2 and diffusion were also used to study stimulated hypoxia in rats. Formation of edema was observed and its effect on corpus

callosum and thalamus were studied, and the effect of induced hypoxia on T_2 values was confirmed with histopathology [42]. T_1 and T_2 were also used to study induced hydrocephalus in rats, and it was observed that T_1 and T_2 increased in white matter, but it was concluded that, although they are related to water content, they cannot be used as direct measures of water content [43]. The T_1 relaxation time was also used to compare the effect of inducing ischemia in rats. T_1 values were higher in the ischemic group (6 subjects) compared to the control group (4 subjects) which also correlated with water content [44].

2. METHODS

2.1 Subjects and Data Acquisition

21 female Wistar rats (mean age: 73.7 ± 7.8 days; weight: 174.1 ± 14.9 g) were scanned using a 7T preclinical MRI (MR Solutions Ltd., Guildford, UK). Motion was prevented by utilizing a head holder accompanied by a bite bar as well as ear canal bars. Anesthesia was done using isoflurane at the levels of 1-2% throughout the scan. Vital signals were also monitored using ECG, respiration, and temperature probes included in Model 1030 (SA Instruments, New York, USA). The work was approved by the ethical committee, and the responsible veterinarian did animal handling.

The protocol lasted around 3 hours for each animal. It included various sequences including T1w (FSE, TR/TE: 1000/11 milliseconds, FA: 90°, Resolution: $0.125 \times 0.125 \times 0.8$ mm^3), T2w (FSE, TR/TE: 2500/40 milliseconds, FA: 90°, Resolution: $0.125 \times 0.135 \times 0.8$ mm^3), IR FLASH (TR/TE/TI: 10/4/50 milliseconds, FA: 8°, Resolution: $0.125 \times 0.25 \times 2$ mm^3), MEMS (TR/TE: 4000/150 milliseconds, FA: 90°, Resolution: $0.16 \times 0.31 \times 1$ mm^3), and Multi gradient echo (MGE) images (TR: 1620 milliseconds, FA: 60°, Resolution: $0.36 \times 0.36 \times 0.36$ mm^3, Min/Max TE: 4/21.12 milliseconds, number of TEs: 9) including magnitude and phase. Figure 2.1 summarizes the process.

2.2 Data Processing and Analysis

Segmentation of ROIs was done using the SIGMA InVivo template as reference. Regions included the white matter, gray matter, ventricles, hippocampus, corpus callosum, and the thalamus. T_1 maps, T_2 maps, and R_2^* maps were computed using the code developed (explained in next sections), whereas QSM maps were generated using Sepia [45]. All of the steps require a brain mask, which is used to extract the brain

and avoid processing irrelevant parts of the images. However, robust tools for brain extraction of small animals are scarce. Therefore, ITK-snap [46] was used with the binary mask provided with the SIGMA atlas to semi-automatically create the initial binary masks for later use in brain extraction. ANTsPy [47], and Nibabel [48] were used as needed for the automatic registration and segmentation of maps, and average values based on various regions of interest were calculated thereafter. One subject was excluded due to cortical malformation, which caused outliers in all maps.

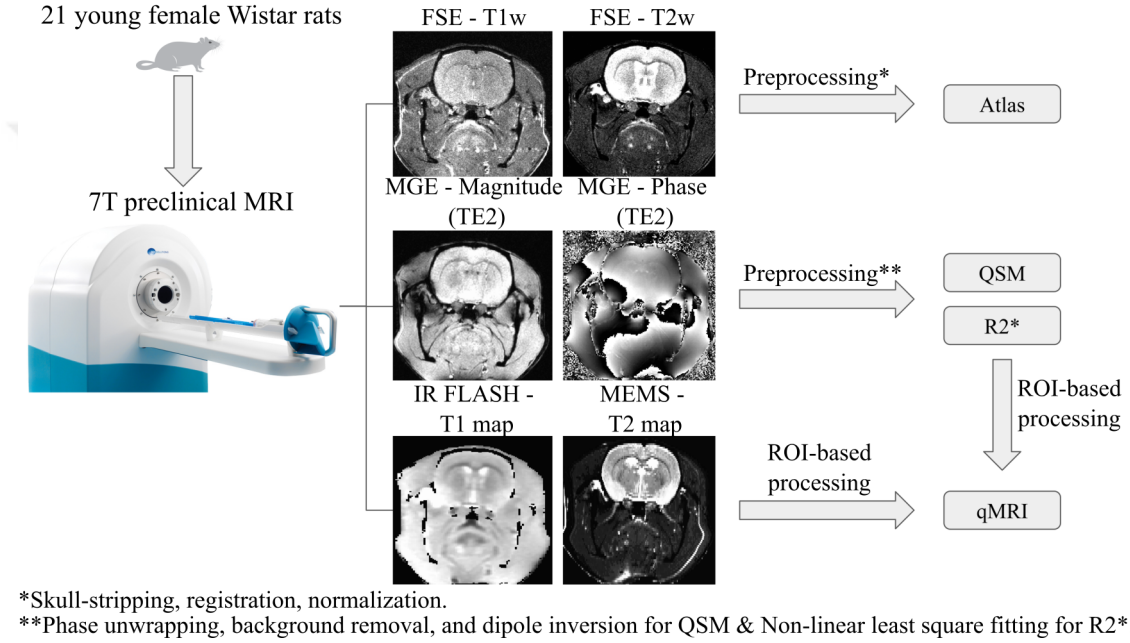

Figure 2.1 The diagram summarizing the protocol used to acquire rat images.

A simple graphical user interface (GUI) was also created using Python's Tkinter library. It enables the user to select the kind of fitting required (T_1, T_2, R_2^*, etc.). It then prompts the user to select the corresponding datasets, and insert the time information (TE for T_2 mapping, TI for T_1 mapping etc.). It is also possible to save the output in the BIDS format explained in the next section, in which case the user is prompted to input the subject number. Finally, an output path (where the user wants the output to be saved) is expected. After completing the fitting and saving the result, a pop-up notifies the user. As all other parts of this work, this was also created on Ubuntu 24.04 LTS using the simple Python version manager PyEnv to isolate working environments and avoid dependency conflicts, and Python 3.12.3 was used unless stated

otherwise.

2.3 Data Management

The brain imaging data structure (BIDS) is a standard/specification for naming and structuring brain imaging data [49]. The specification requires for qMRI data to have the directory tree shown in Figure 2.2.

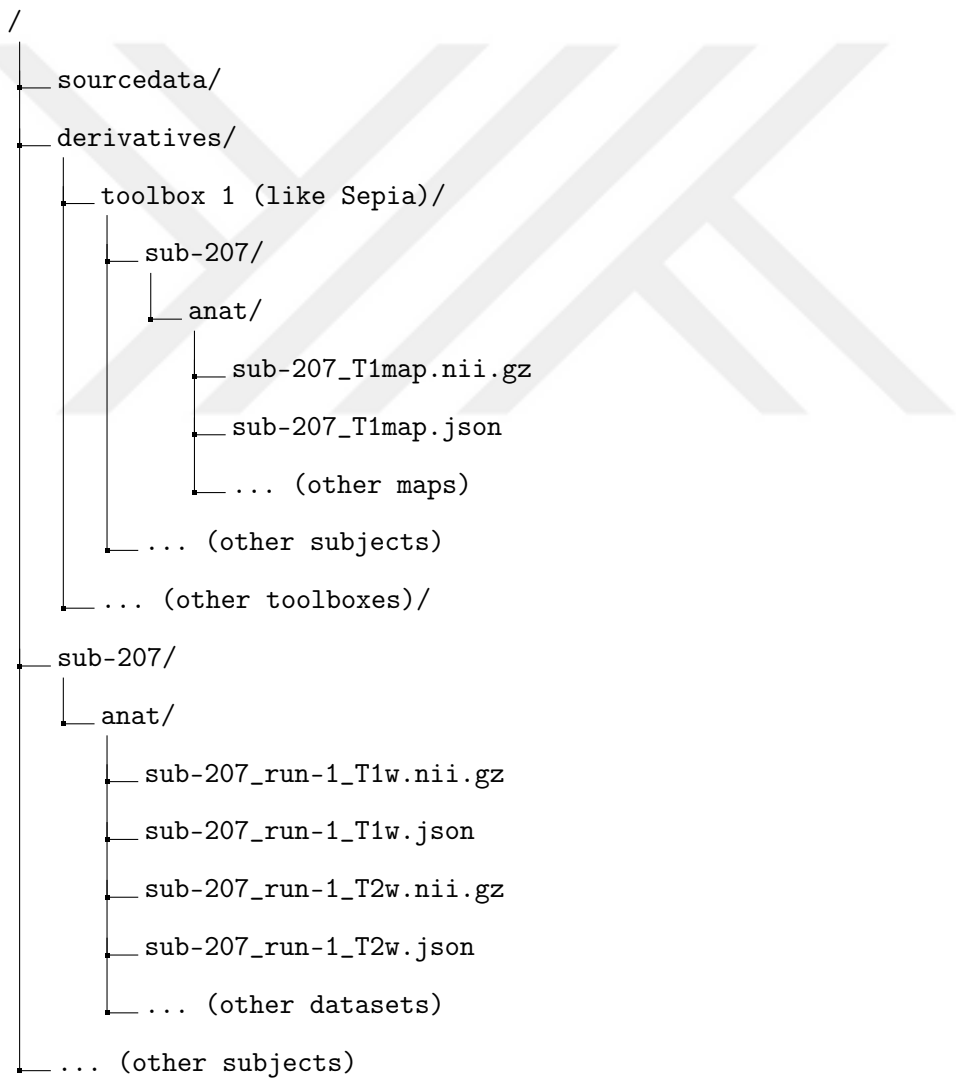

Figure 2.2 Directory structure of the dataset following BIDS and derivative outputs.

The `sourcedata/` should contain the raw DICOM images as well as any other

raw data (like behavioral). The `dcm2niix_afni` function was used to first convert all DICOMs to the Nifti format. Then the script `decin.tcsh` (a bash script that uses AFNI functions) is used to correct the orientation of the datasets. Each subject's data was stored in its directory under the root directory. For example, all datasets of `sub-207` are stored in `sub-207/anat/`. All other derived quantitative maps should be stored in the `derivatives` directory. For example, if the quantitative susceptibility map of `sub-207` was derived using Sepia, it should be stored in `derivatives/Sepia/sub-207/anat/`.

It also provides specifications for naming quantitative MRI datasets. The raw data that we have and that the specification applies to is of three types: Inversion Recovery (IR), Multi-Echo Multi-Slice (MEMS), and Multi-Echo Gradient Recalled Echo (MEGRE). The specification requires the naming of the datasets to be as shown in Figure 2.3.

```
/
└── sub-207/
    └── anat/
        ├── sub-207_run-1_echo-<index>_part-<mag|phase|real|imag>_MEGRE.json
        ├── sub-207_run-1_echo-<index>_part-<mag|phase|real|imag>_MEGRE.nii.gz
        ├── sub-207_run-1_echo-<index>_part-<mag|phase|real|imag>_MESE.json
        ├── sub-207_run-1_echo-<index>_part-<mag|phase|real|imag>_MESE.nii.gz
        ├── sub-207_run-1_inv-<index>_part-<mag|phase|real|imag>_IRT1.json
        └── sub-207_run-1_inv-<index>_part-<mag|phase|real|imag>_IRT1.nii.gz
```

Figure 2.3 The required naming style of relevant datasets according to the BIDS specification.

It should be noted that:

- IRT1 is the BIDS specification's label for Inversion Recovery datasets used for T_1 mapping (IR FLASH in the files produced by the scanner), MESE is the label for Multi-echo Spin Echo (MEMS in the files produced by the scanner), and MEGRE

is the label for Multi-echo Gradient Recalled Echo (MGE in the files produced by the scanner).

- `part` is used to indicate different reconstructions of the same scan. For example, in the case of MEGRE; phase, magnitude, real, imaginary, and SWI are provided.

- `echo` and `inv` are used to indicate the number/index of the echo/inversion time, not the echo/inversion time, of an individual image acquired at a particular echo/inversion. This is because the BIDS specification requires that 4D datasets are converted into a group of separate 3D volumes, with each echo/inversion separated. For example, our MEGRE datasets have 9 echos, so we should have 9 MEGRE datasets with corresponding json sidecars.

The last item listed above makes it impractical because our datasets have 128 inversion times in the IRT1 images, 9 echos for MEGRE images, and 10 echos for MESE images. So, what I did instead was to combine each group of echos into a 4D dataset (echos of the same scan of course), and correct the TE and TI information in the Nifti headers of the datasets (the `toffset` and `TE`/`TI` fields). Also, I added the full TE and TI vectors as extensions to the Nifti headers and in the json sidecars. The TE and TI information is extracted automatically from the corresponding DICOM files. However, it is possible to also do it the other way, that is to separate echos as the BIDS format requires. Finally, the BIDS Validator was run to validate compliance.

2.4 Relaxometry

As reviewed until Section 1.4, after excitation of the imaged volume, spins start a process of so-called relaxation in which they go back to equilibrium. As they are doing so, they produce a detectable signal, which is detected using coils in the MRI scanner. This process is described by the Bloch equation (Eq. 1.42), and it is possible to derive signal models of each relaxation type.

2.4.1 T_1 Mapping

Eq. 1.54 describes the general relaxation of the longitudinal component. However, as mentioned previously, the signal model used to derive the quantitative map depends on the sequence used. The sequence used in this work is Inversion Recovery Fast Low Angle Shot (IR FLASH) [50]. Therefore, T_1 relaxation can be modeled using the following equation:

$$S(TI) = A - Be^{-TI/T_1^*} \tag{2.1}$$

Where TI is the time to inversion. This gives the apparent T_1 or T_1^*. To get T_1, the following correction needs to be done:

$$T_1 = T_1^* \times \left(\frac{B}{A} - 1\right) \tag{2.2}$$

However, IR-FLASH sequence used for T_1 fitting requires polarity restoration before fitting [51]. It is only possible to fit the model after polarity restoration. This involves reversing the polarity (i.e. multiplying by -1) of all the points before the minimum point (refer to Figure 2.4 for explanation) in a given voxel's signal in two ways: 1) excluding the minimum point, and 2) including the minimum point. Then the residual is calculated for each case, and the combination that gives the least error is preferred. Levenberg-Marquardt (LM) optimization is usually used for such fitting tasks, but it requires a priori knowledge of possible T_1 values for initialization. Another method also exists that requires no initialization but uses grid search between possible T_1 values in biological tissue, namely reduced dimension non-linear least squares (RD-NLS) [51]. In this work, scipy.optimize.curve_fit() was used, which employs the Levenberg-Marquardt (LM) approach by default.

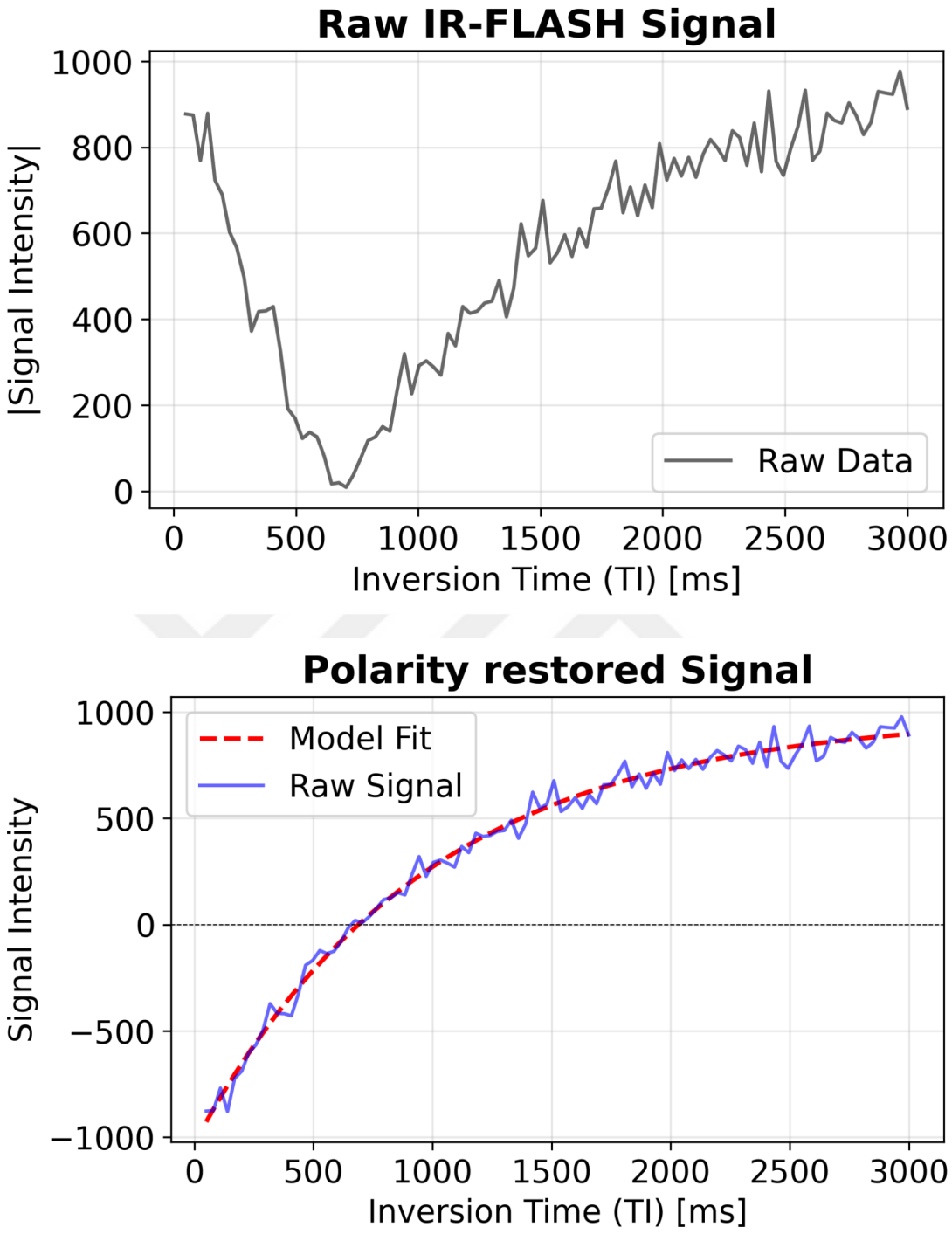

Figure 2.4 Polarity restoration before fitting the exponential. The absolute value of the raw signal (above) gives the raw signal which is fitted (below).

2.4.2 T_2 Mapping

The spin system nuclear spin vector has multiple components, and T_1 describes the relaxation of the z-component. Another component is the transverse component, which is described by the time constant T_2. Using Eq. 1.57, the following model can be used with multi-echo spin-echo images:

$$S(TE) = Ae^{-TE/T_2} \tag{2.3}$$

Where TE is time to echo. The acquired signal can be fitted by defining the model and using scipy.optimize.curve_fit().

2.4.3 R_2^* Mapping

When GRE is used for imaging, spins are also affected by inhomogeneities and by interactions with other spins, which speeds up the process of transverse relaxation. So, shortened transverse relaxation time T_2^* becomes:

$$\begin{aligned} \frac{1}{T_2^*} &= \frac{1}{T_2'} + \frac{1}{T_2} \\ R_2^* &= R_2' + R_2 \end{aligned} \tag{2.4}$$

Where R is rate and is measured by Hz. So, the model becomes:

$$\begin{aligned} S(TE) &= Ae^{-TE/T_2^*} \\ S(TE) &= Ae^{-TE \times R_2^*} \end{aligned} \tag{2.5}$$

Therefore, R_2^* maps can be computed by fitting an exponential to the GRE magnitude data. This can be easily done with scipy.optimize.curve_fit().

2.4.4 Reliability Estimates for Relaxometry

Bland-Altman test was run for a single subject as a sanity-check to compare the outcome of the developed code to outcomes of other toolboxes used in literature. qMRLab was used to generate T_1 and T_2 maps. qMRLab has the option inversion recovery (IR) for T_1 maps, which uses the signal model $A - Be^{-TI/T_1}$. For T_2 maps, the mono-exponential model was used, but the version of the software used had a bug and the fitting could not be performed. So, instead of using the standard model Ae^{-TE/T_2}, another option which converts the problem to a linear problem using natural logarithms was used. For R_2^*, Sepia was used with the non-linear least squares fitting option. Then, using the same ROI masks, paired measurements were used to find the difference for each ROI, then the average and standard deviation of the differences was calculated (the mean is called bias). Finally, lines of bias ± 2×standard deviations were plotted together with the differences for each measurement.

To also better understand how reliable the calculated ROI mean for each parameter is, standard error of mean (SEM) was used, which is calculated as

$$SEM_{ROI} = \frac{\sigma_{ROI}}{\sqrt{N-1}} \tag{2.6}$$

where σ_{ROI} is the standard deviation for the ROI at hand, and N is the number of voxels used in the calculation. Distributions of SEM for each ROI and parameter was then plotted as violin plots.

2.5 QSM

2.5.1 Validation Using Rat Susceptibility Phantom

A challenging aspect of optimizing susceptibility mapping pipelines for specific applications/datasets is the ambiguity of ground truth. To overcome this, a ground truth phantom was created using the high resolution multicontrast Wistar rat brain

atlas [52]. The atlas includes labels, scalar images derived from diffusion data (like Fractional Anisotropy), and susceptibility maps. To create the phantom, labels were used to calculate the mean for each label and assign the mean value to it, thus producing a susceptibility ground truth. Smoothing was applied using a Gaussian filter with a standard deviation of 0.42, and air susceptibility was set to 0.398 ppm [22]. Then, the total field was simulated by convolving the synthetic susceptibility reference with the dipole kernel, and the resultant image was used to evaluate mainly three dipole inversion algorithms: TKD [23], iLSQR [24], and STAR-QSM [26]. nRMSE (root mean square deviation after subtracting the whole brain mean) was used as a comparison metric and was calculated as

$$RMSE = \sqrt{\frac{1}{N}\sum_{i=1}^{N}(I_{p,i} - I_{r,i})^2} \tag{2.7}$$

where $I_{p,i}$ and $I_{r,i}$ are calculated and real susceptibility values -after demeaning- for voxel i, respectively. STAR-QSM was found to give the best results (nRMSE and visual inspection - refer to Results for details) and was used for the preprocessing of the data.

2.5.2 Echo Combination

Phase accumulates with time as shown in Eq. 1.49, and more echoes mean better contrast. So, in multi-echo GRE, multiple echoes are combined. Various approaches to do so exist. For example, the optimum weights approach uses information from the magnitude image. Here we use weighted phase increment (WPI) [53]. Combination of different echoes is done as follows:

$$WPI_w = angle\left(\frac{1}{N-1}\sum_{n=1}^{N-1} S_n^* S_{n+1}\right) \tag{2.8}$$

Where S_n^* is the conjugate of S_n, the complex phase value at time n.

2.5.3 Phase to Susceptibility

Phase unwrapping was then done using the Laplacian operator. Figure 2.5 shows an example of the input and output for this step. It is visible that the discontinuities are removed using the Laplacian operator. Consecutively, after eroding one voxel be-

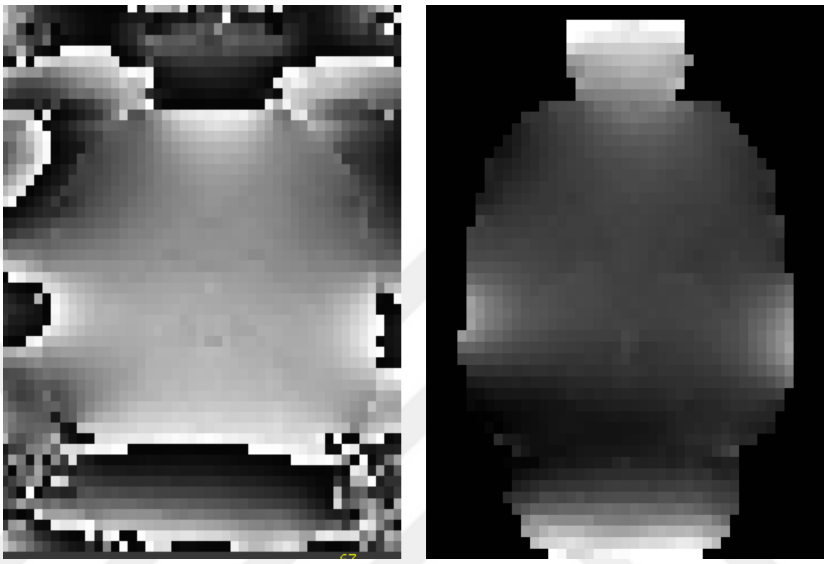

Figure 2.5 Phase wraps in the raw phase image (left) are removed using the Laplacian operator to yield a total field image (right).

fore background field removal, V-SHARP was applied [22] with a variable kernel size between 1 mm and 12 mm, producing the internal field as seen in Figure 2.6. Finally,

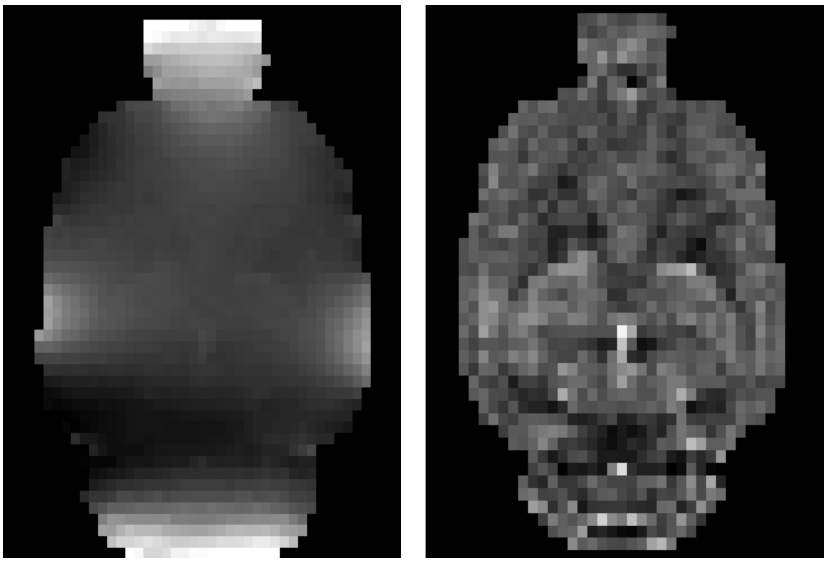

Figure 2.6 v-SHARP removes the background field from the total field image (left) and produces an internal field image (right - display range [-8 8] rad).

STAR-QSM was used for dipole inversion [26] to avoid streaking artifacts. Susceptibility values were then referenced to white matter and ROI-based values were plotted. Figure 2.7 shows how the internal field is converted to a quantitative susceptibility map after dipole inversion.

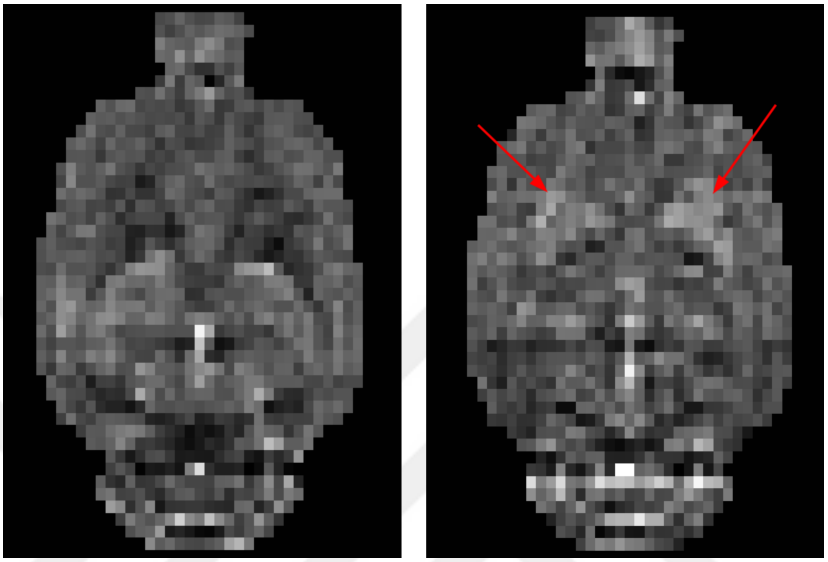

Figure 2.7 Dipole inversion deconvolves the dipole kernel with the internal field image (left - display range [-8 8] rad) to yield a quantitative susceptibility map (right - display range [-0.08 0.08] ppm). It is possible to see deep brain structures in the susceptibility map, shown with red arrows.

3. RESULTS

3.1 Toolbox Utilities

The GUI is presented in Figure 3.1. PyEnv is first used to activate the virtual environment called "ThesisWork." This is done to avoid dependency conflicts and isolate working environments, the version of Python in that environment is then shown using the command `python --version`. Finally, the GUI is run using the command `python GUI.py` where `GUI.py` is where the GUI script is written. The GUI is then visible, and filling required fields is followed by running the fitting. Outputs of functions inside the code that require printing is returned in the terminal, and a pop-up notifies the user when the fitting is over. Figure 3.2 shows the result of running the BIDS validator on the official GitHub repository. The errors are missing fields that are required, whereas warnings are due to missing fields that are recommended but not necessarily required. This was followed by quantitative mapping for the different parameters mentioned earlier.

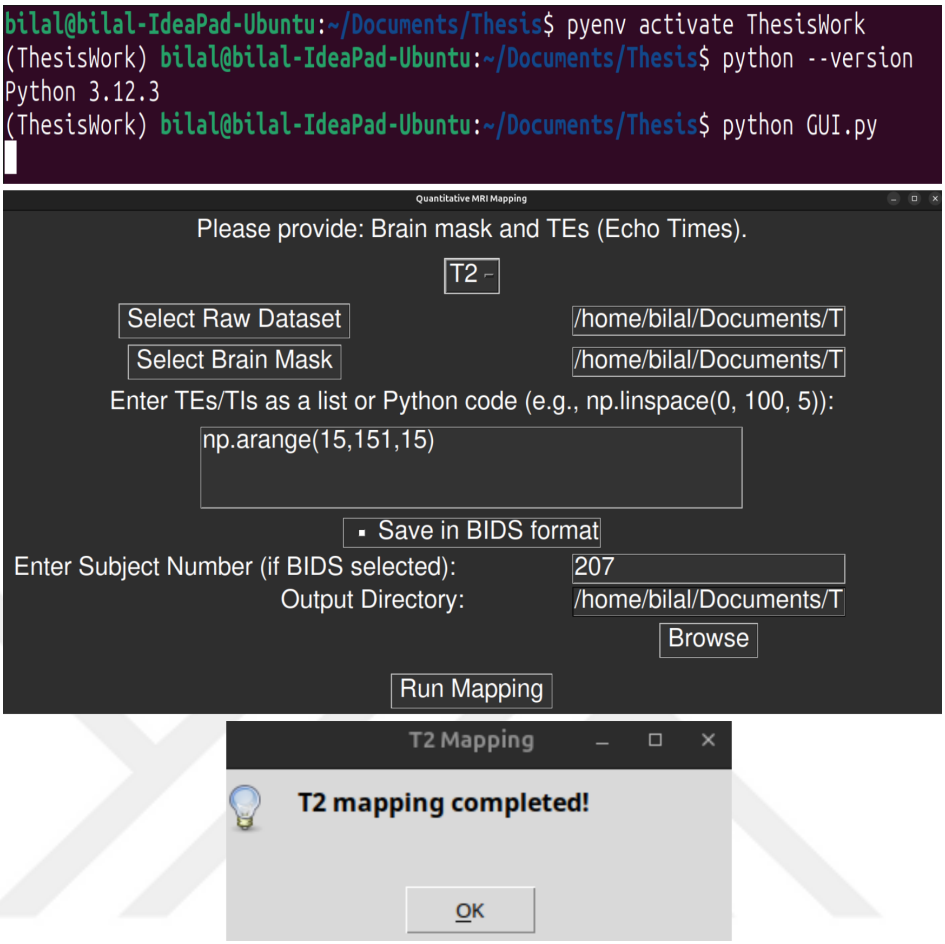

Figure 3.1 Depiction of how the GUI works. Starting on the top, the virtual environment is activated, then the GUI is run. The necessary datasets are selected, and the fitting is started. A pop-up notifies the user when the fitting is over.

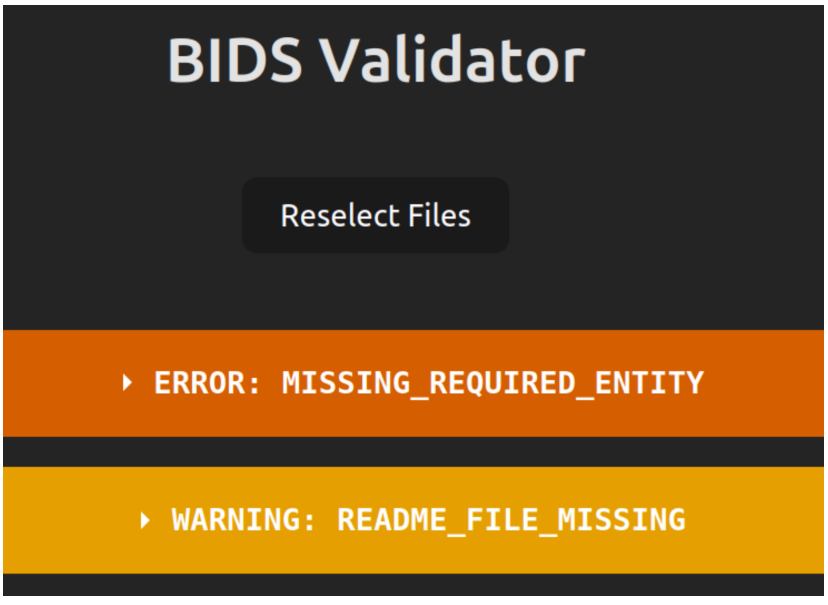

Figure 3.2 Result of running the BIDS validator.

3.2 Validation Using a Preclinical Phantom

Figure 3.3 shows the reference susceptibility. Convolution of the reference volume with the dipole kernel yields the total field shown in Figure 3.4. Table 3.1 shows computation time and nRMSE scores of each threshold used in TKD, and Figure 3.5 shows the corresponding maps. Table 3.2 shows computation time and nRMSE scores of TKD, iLSQR, and STAR-QSM. Corresponding maps are shown in Figure 3.6.

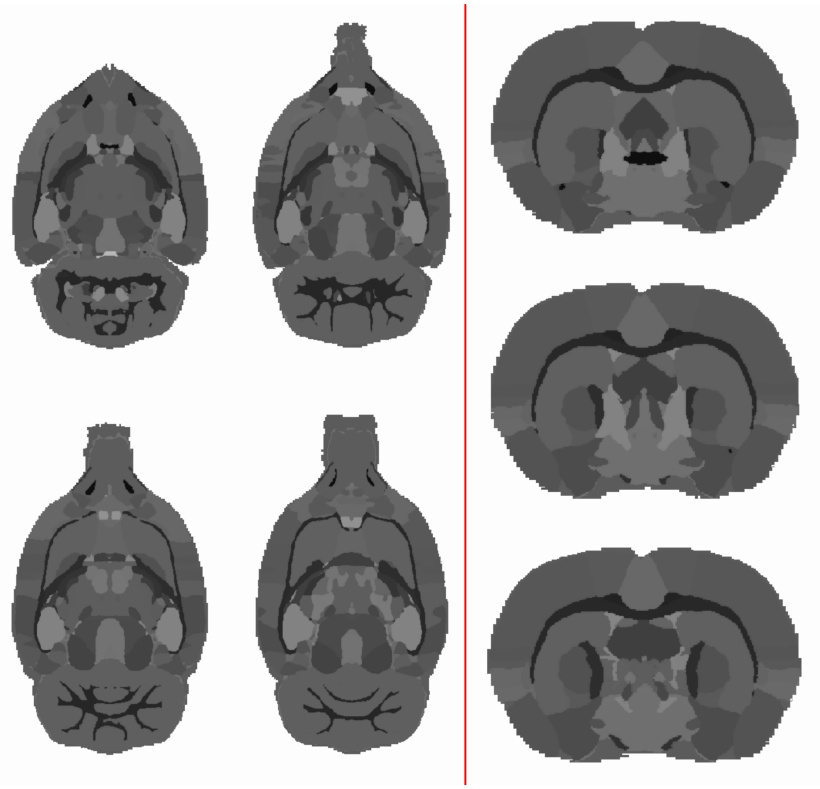

Figure 3.3 Multiple Axial (left) and Coronal (right) slices from the reference susceptibility phantom (display range [-0.05 0.05] ppm).

Table 3.1
Time taken for different thresholds used with TKD with the corresponding nRMSE score.

ε	0.15	0.20	0.25	0.30	0.35	0.40
Time (s)	5.48	5.13	4.98	4.79	4.51	4.48
nRMSE (ppm)	0.01617	0.01530	0.01436	0.01326	0.01170	0.01149

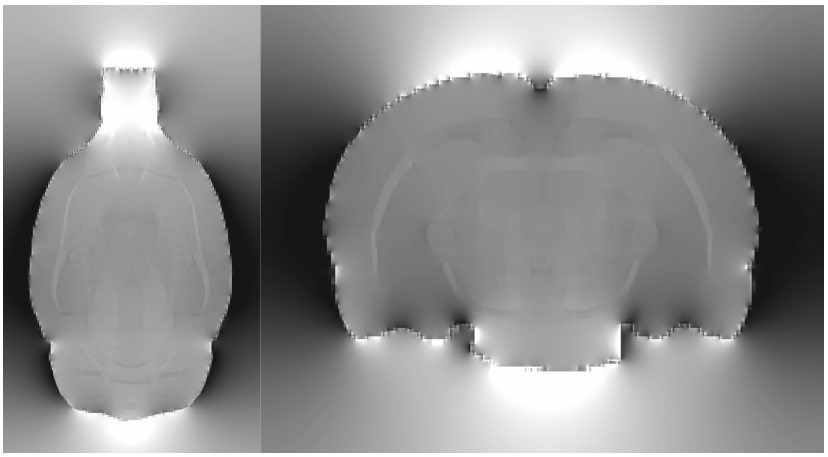

Figure 3.4 Axial (left) and Coronal (right) views of the total field after convolving the reference susceptibility volume with the dipole kernel.

Table 3.2
Time taken for each of the algorithms together with its nRMSE score.

	TKD	iLSQR	STAR-QSM
Time (s)	5.48	5982	87
nRMSE (ppm)	0.01617	0.01885	0.01633

3.3 Multiparametric Quantitative Maps

Figures 3.7 - 3.10 show examples of the quantitative maps produced in this analysis. A single slice was acquired for T_1 mapping, and it can be seen in Figure 3.7, and it is possible to see the corpus callosum as well as other distinct structures. Multiple slices were acquired for T_2 mapping, so multiple slices from the coronal view is shown in Figure 3.8 where it is possible to see corpus callosum, but also other structures. The axial view is preferred for both QSM and R_2^* in Figures 3.9 and 3.10 because it is easier to see deep brain structures. These show images from a single subject, and Table 3.3 shows a summary of mean values for each parameter in the different regions of interest examined as mean $\pm$ standard deviation across all subjects.

To get a sense of how the data is distributed, Figure 3.11 shows the distribution of mean T_1 relaxation times for each ROI. Five regions of interest were examined because of the location of the slice chosen. More regions were included in T_2 mapping (Figure 3.12), R_2^* mapping (Figure 3.13), and QSM (Figure 3.14) since a larger volume

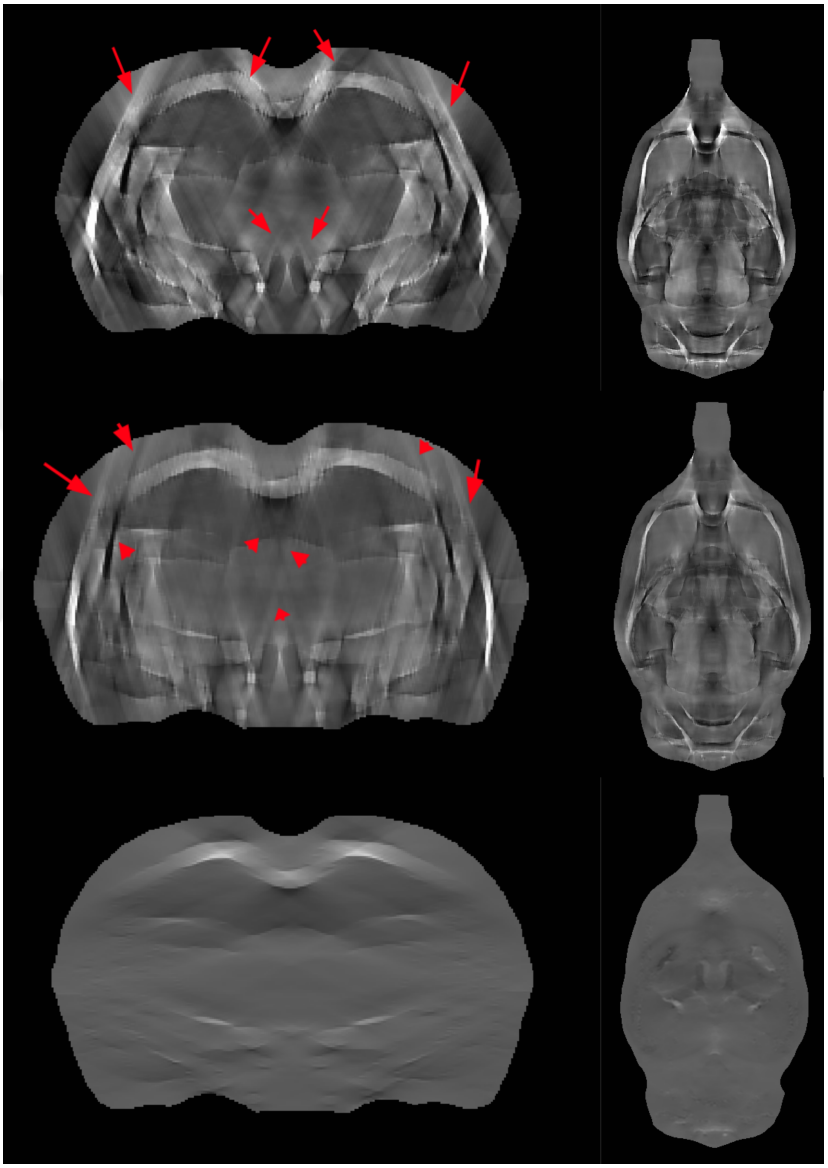

Figure 3.5 The result of using TKD with an ε value of 0.15 (uppermost), 0.25 (middle), and 0.4 (lowermost). Display range is [-0.03 0.03] ppm for all maps. Red arrows highlight the so-called streaking artifacts.

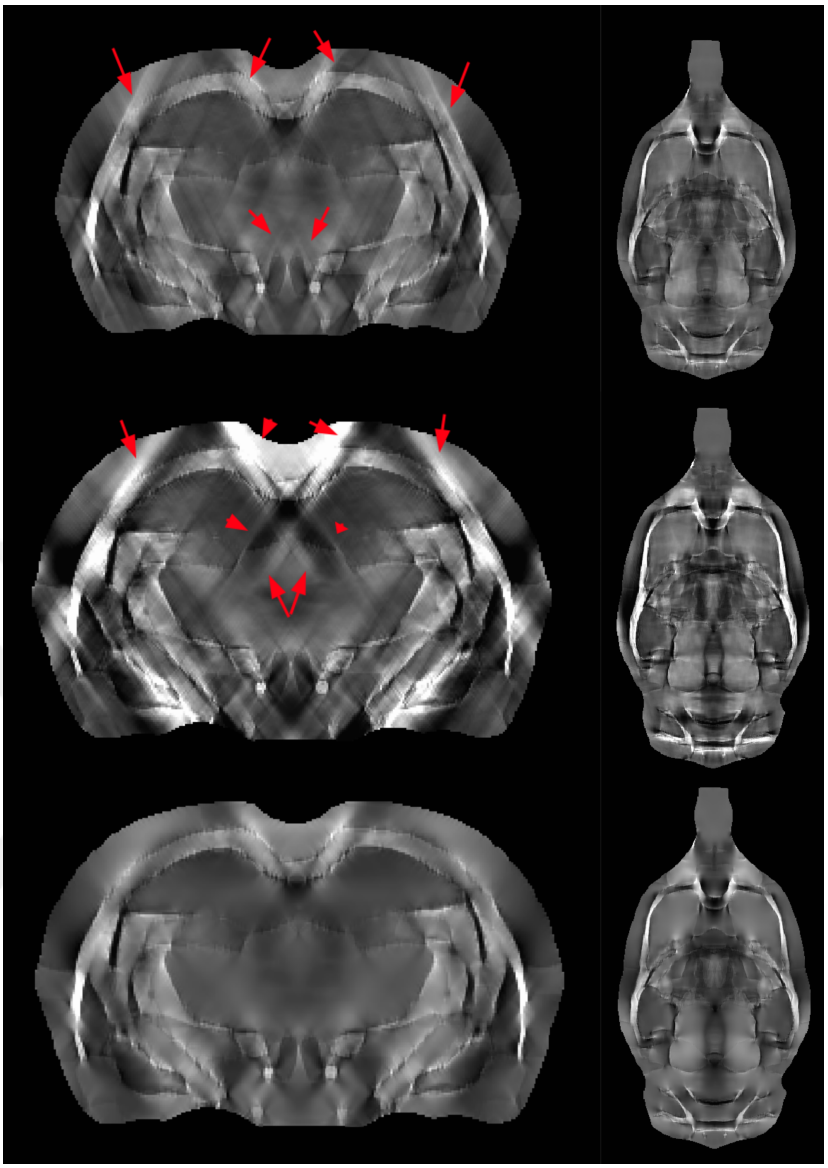

Figure 3.6 The result of using TKD with an ε value of 0.15 (uppermost), iLSQR (middle), and STAR-QSM (lowermost). Display range is [-0.03 0.03] ppm for all maps. Red arrows highlight streaking artifacts.

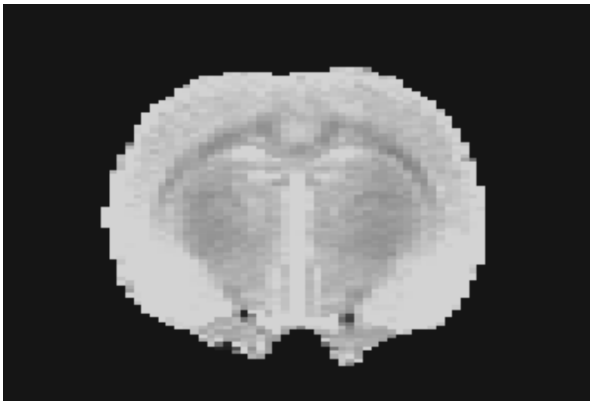

Figure 3.7 An exemplary quantitative T_1 map produced by fitting the signal model defined previously to raw data (coronal view - display range [0 1700] ms).

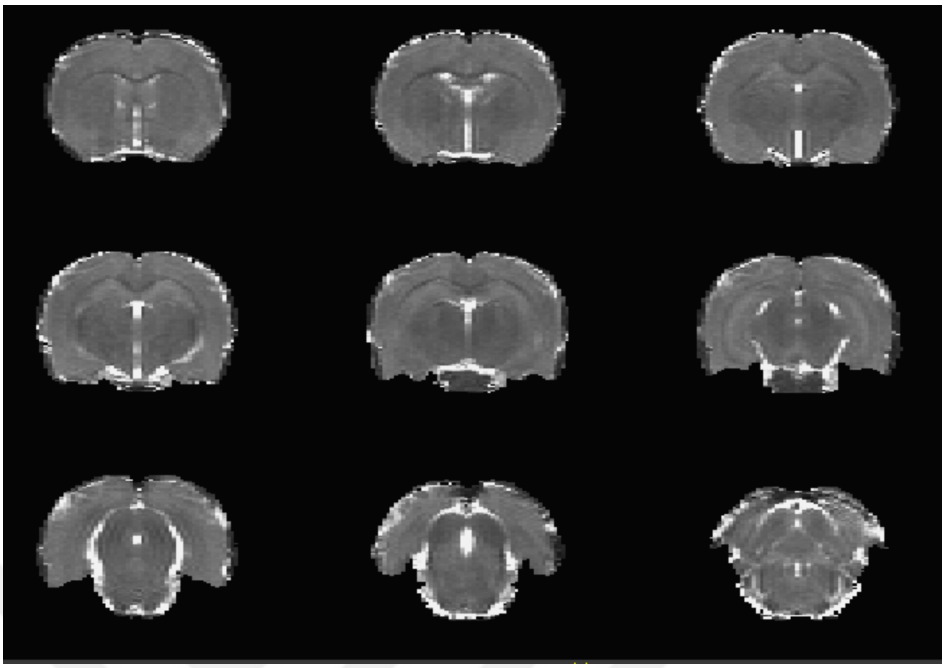

Figure 3.8 Exemplary slices of a T_2 map produced in this analysis (coronal view - display range [0 100] ms).

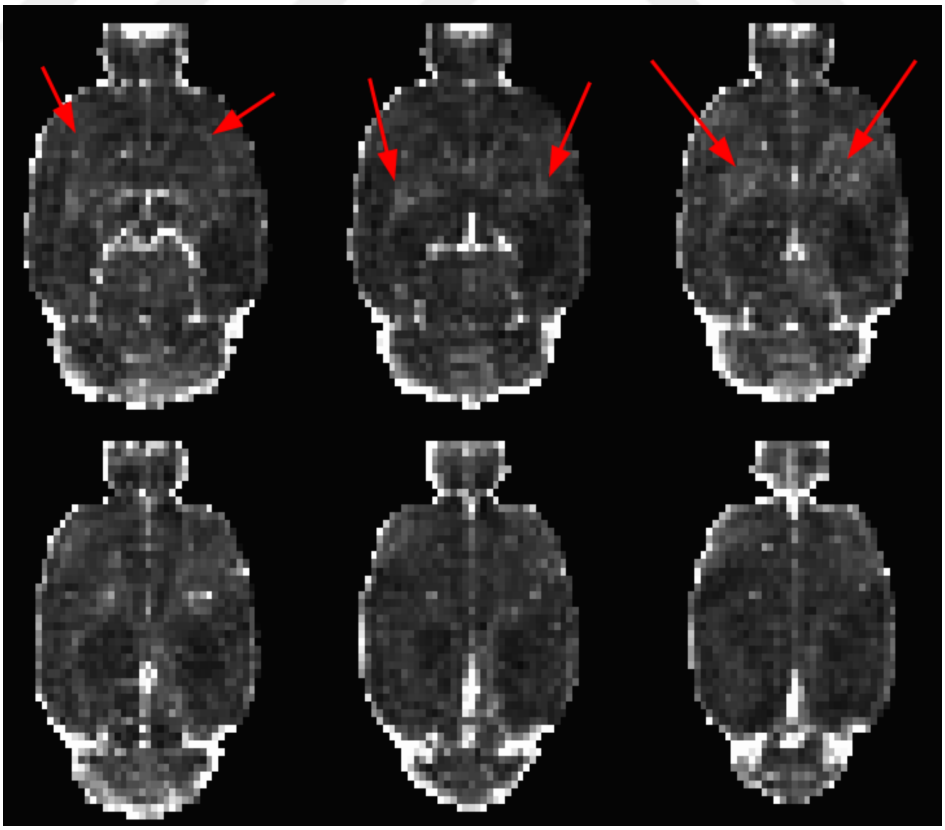

Figure 3.9 Exemplary slices of an R_2^* map produced in this analysis (axial view - display range [0 80] Hz). It is possible to see deep brain structures shown with arrows.

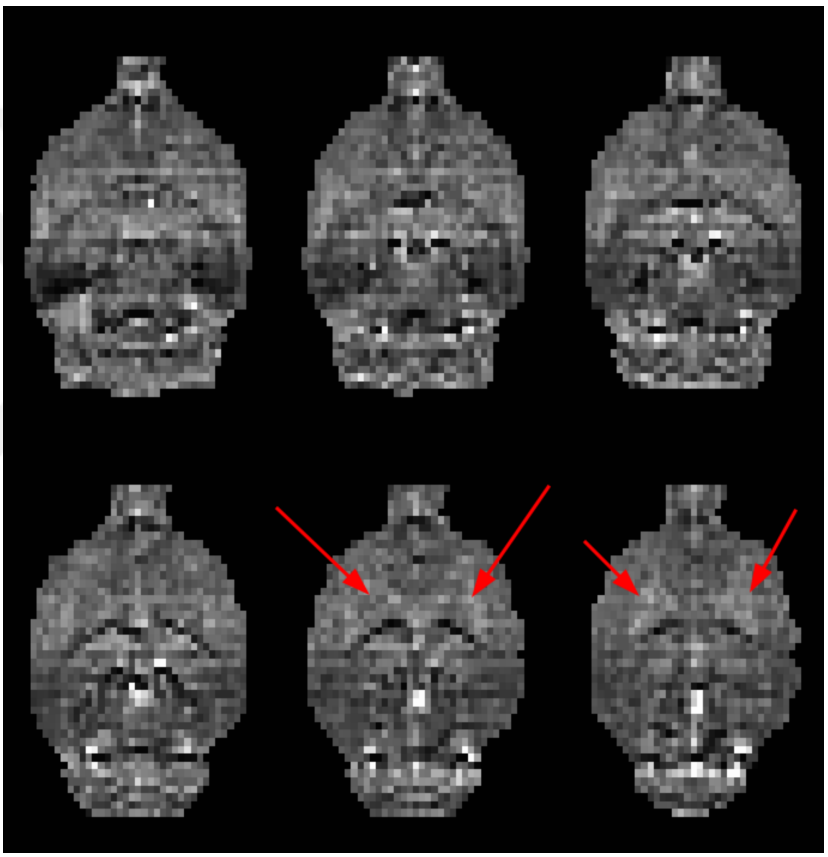

Figure 3.10 Exemplary slices of a quantitative susceptibility map produced in this analysis (axial view - display range [-0.08 0.08] ppm). It is possible to see deep brain structures shown with arrows.

Table 3.3
Average values of different quantitative parameters in different brain regions.

ROI	QSM (ppm)	R_2^* (Hz)	T_2 (ms)	T_1 (ms)
GM	-0.00176 ± 0.00096	35.54 ± 1.15	63.33 ± 1.05	1624.90 ± 37.57
WM	Reference	36.53 ± 2.36	64.23 ± 2.078	1541.28 ± 54.44
Ventricles	-0.00686 ± 0.00983	27.23 ± 5.39	99.54 ± 30.01	1702.94 ± 61.95
CC	0.00155 ± 0.0014	29.49 ± 1.55	60.75 ± 3.1	1543.12 ± 63.64
Thalamus	0.01452 ± 0.00205	27.71 ± 0.79	56.19 ± 1.49	1501.76 ± 52.23
Hippocampus	0.00994 ± 0.00371	35.13 ± 3.22	70.30 ± 24.42	X
GP	0.0025 ± 0.01058	27.42 ± 2.53	55.48 ± 2.55	X
Striatum	0.00329 ± 0.00178	25.77 ± 1.08	59.64 ± 1.40	X

is chosen. Each blue dot is a single measurement from one subject, The horizontal orange line is the median, and the starting and end of each blue box are the 1^{st} and 3^{rd} quartiles (Q_1 and Q_2), respectively. The whiskers mark the farthest points from the Q_1 and Q_3 quartiles that are within the range of $1.5 \times IQR$ where $IQR = Q_3 - Q_1$ (the range or the blue box). Only non-zero values were used in all plots and calculations.

Figures 3.15 - 3.17 show the results for the Bland-Altman test, which was run as a sanity check for a single subject. Bias is the average difference between the measurements of the two toolboxes. The x-axis show the average measurement for each point, and the y-axis shows the difference for that point as well. Limits are set as twice the standard deviation of the difference between the two toolboxes. For T_1 and T_2, measurements are in milliseconds (ms), whereas for R_2^* it is in Hz. Figures 3.18 - 3.20 show ordered bar plots of voxel counts per ROI for MEGRE (QSM and R_2^*), T_1, and T_2, respectively. QSM and R_2^* were combined because the same masks and same MEGRE data was used (magnitude for R_2^* and phase for QSM). Voxel counts from each subject were also used to calculate the standard error of mean (SEM) for each subjet and ROI, and the distributions of SEM for each ROI are shown as violin plots in Figures 3.21 for QSM, 3.22 for T_1, and 3.23 for T_2 values.

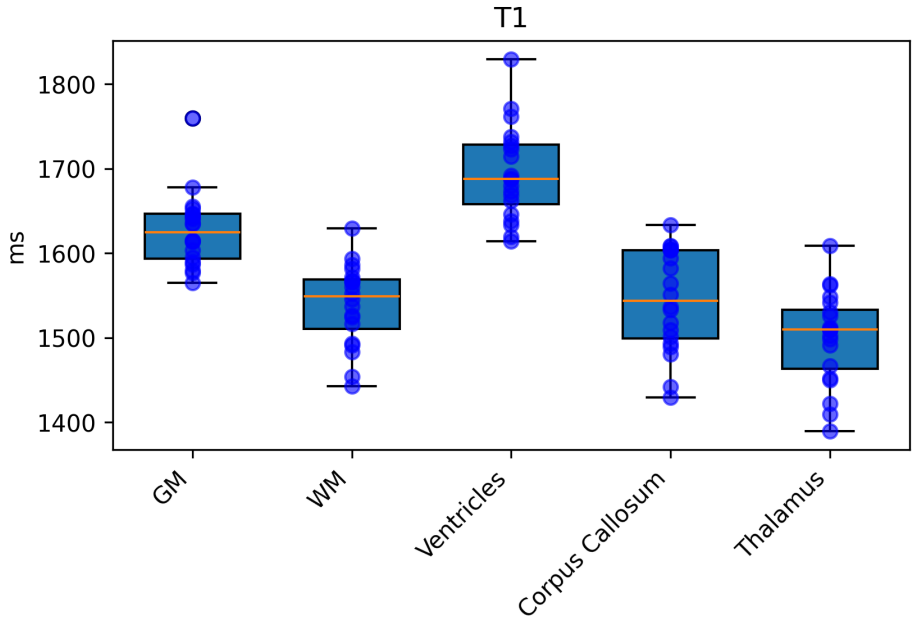

Figure 3.11 Box plot of the average T_1 relaxation times for the examined regions of interest (ROIs).

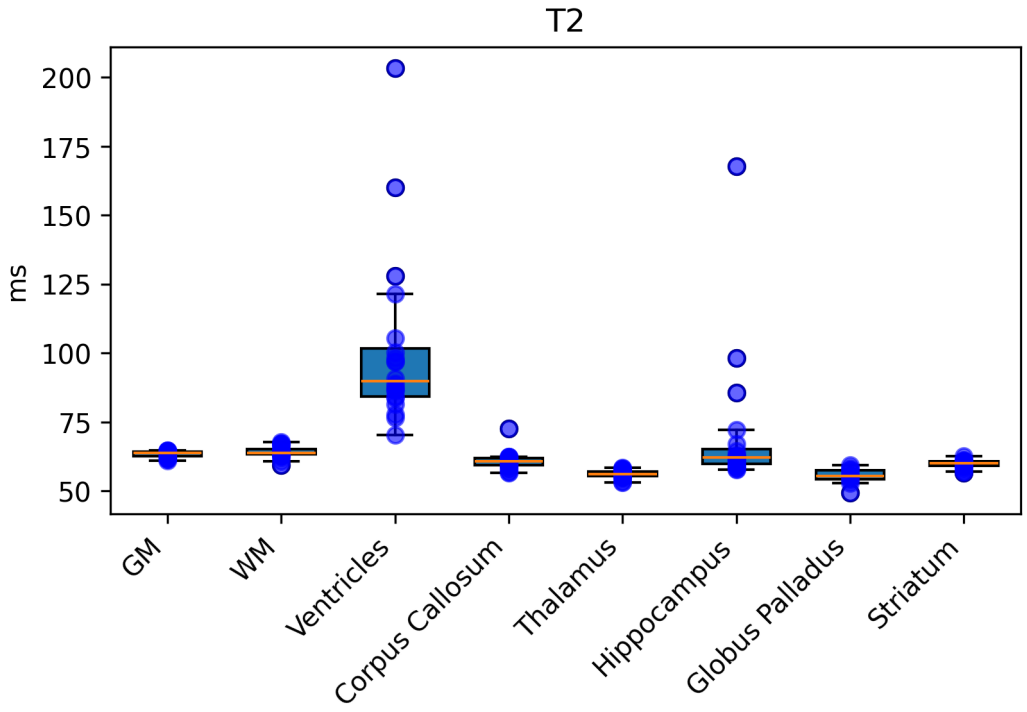

Figure 3.12 Box plot of the average T_2 relaxation times for the examined regions of interest.

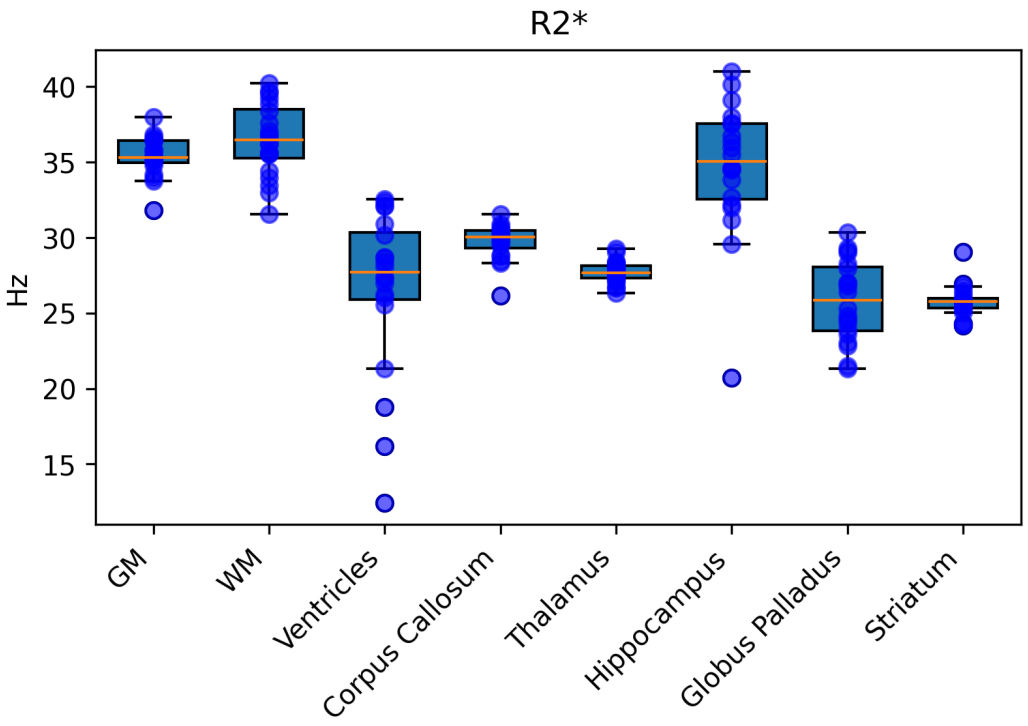

Figure 3.13 Box plot of average R_2^* relaxation rates for the examined regions of interest.

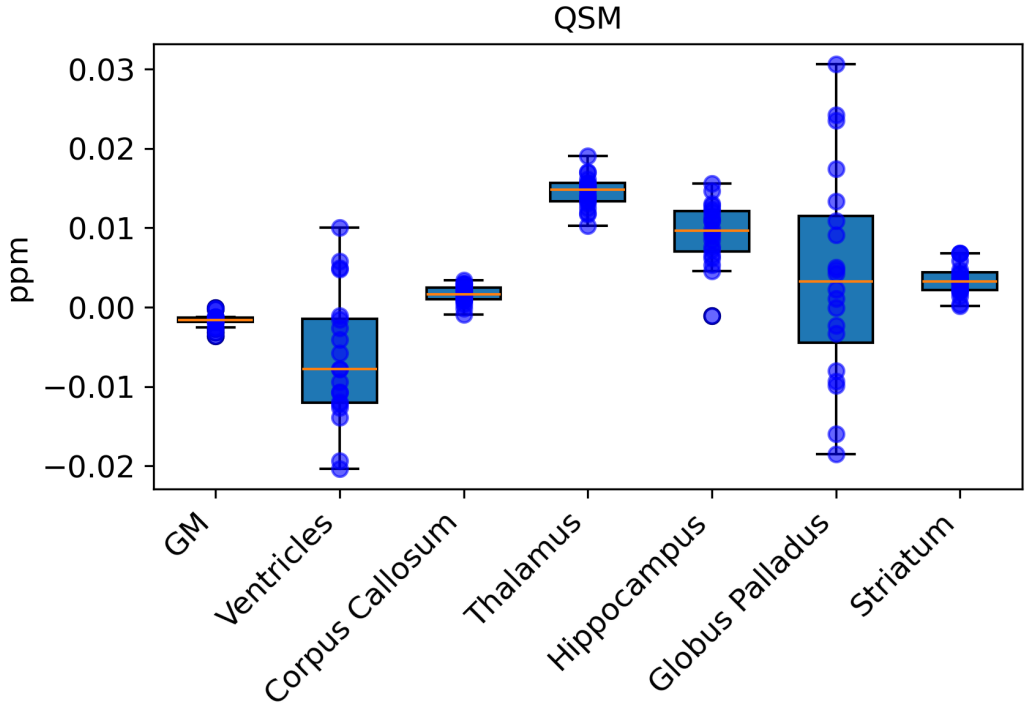

Figure 3.14 Box plot of average susceptibility values for the examined regions of interest.

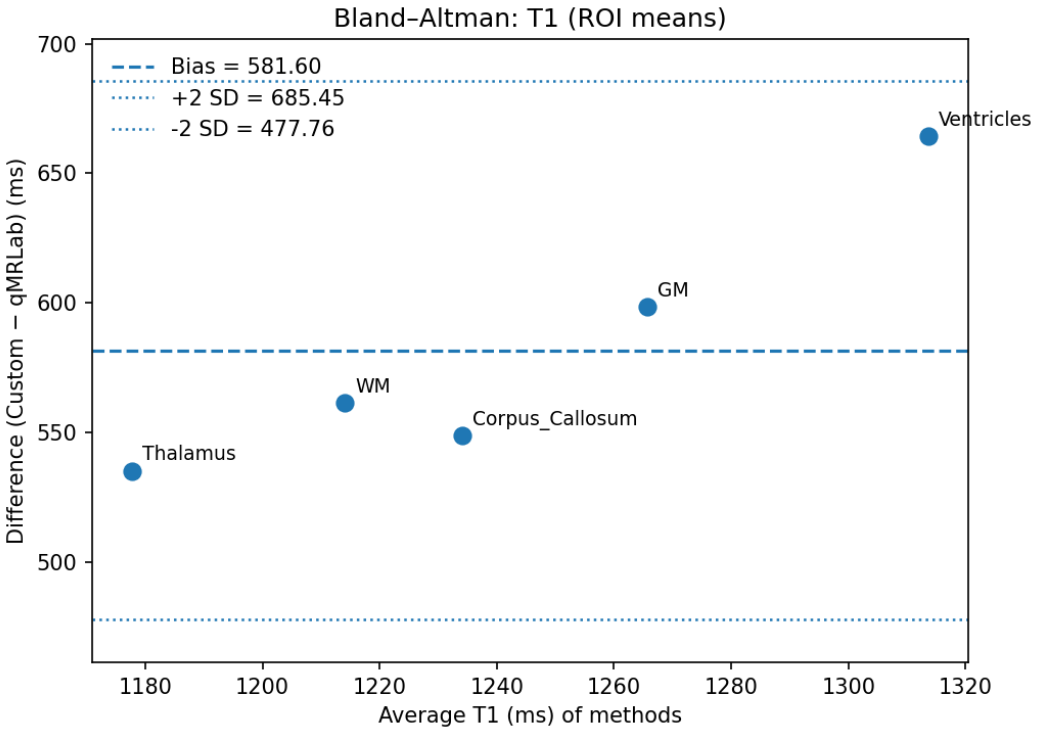

Figure 3.15 Bland-Altman test for T_1 values for a single subject as a sanity check.

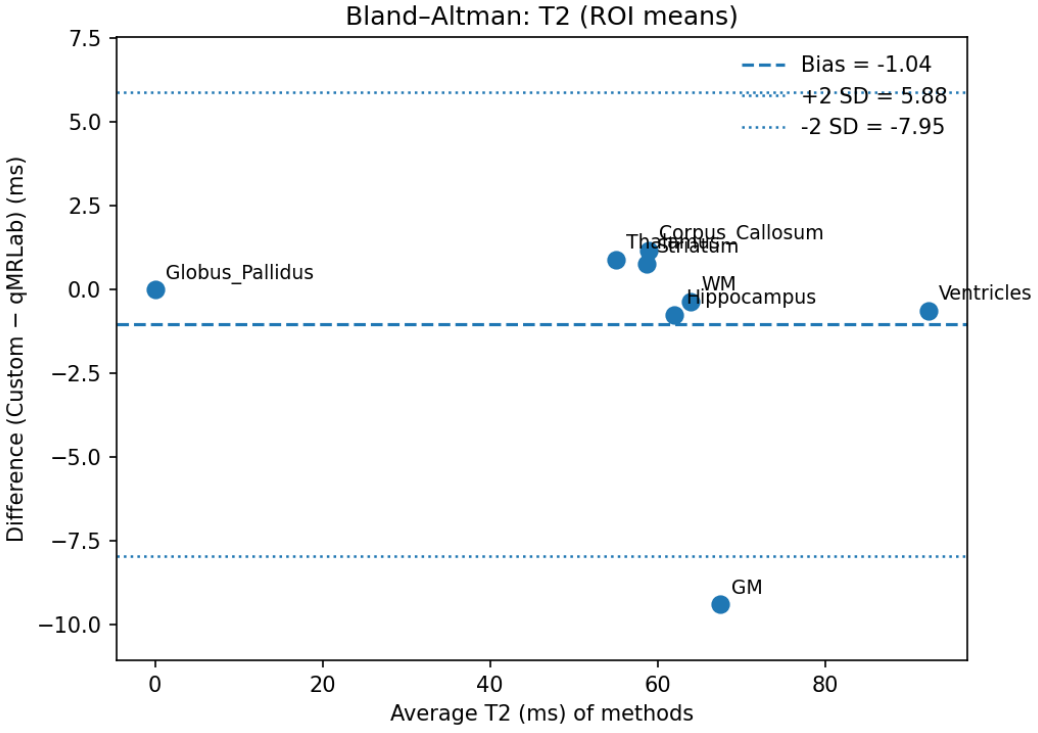

Figure 3.16 Bland-Altman test for T_2 values for a single subject as a sanity check.

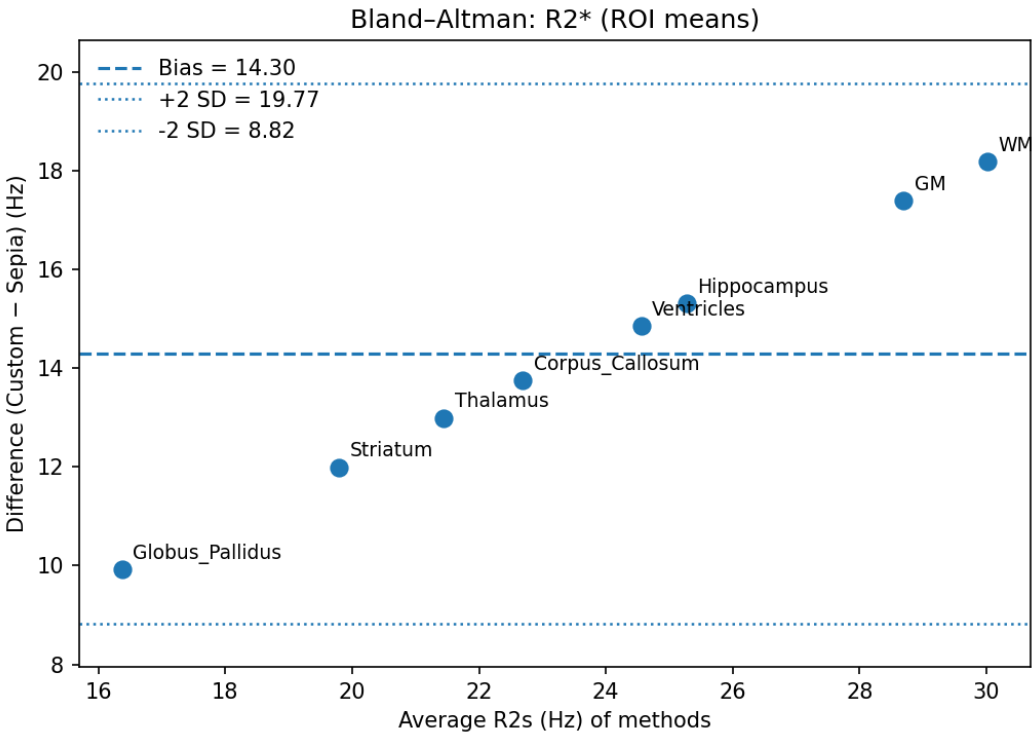

Figure 3.17 Bland-Altman test for R_2^* values for a single subject as a sanity check.

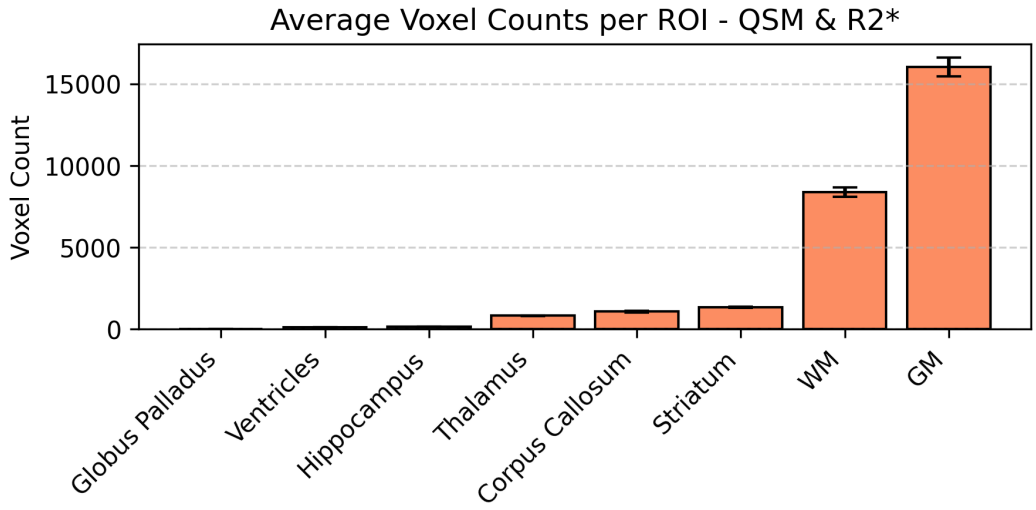

Figure 3.18 Average voxel count for each region of interest for MEGRE images used in R_2^* and quantitative susceptibility mapping.

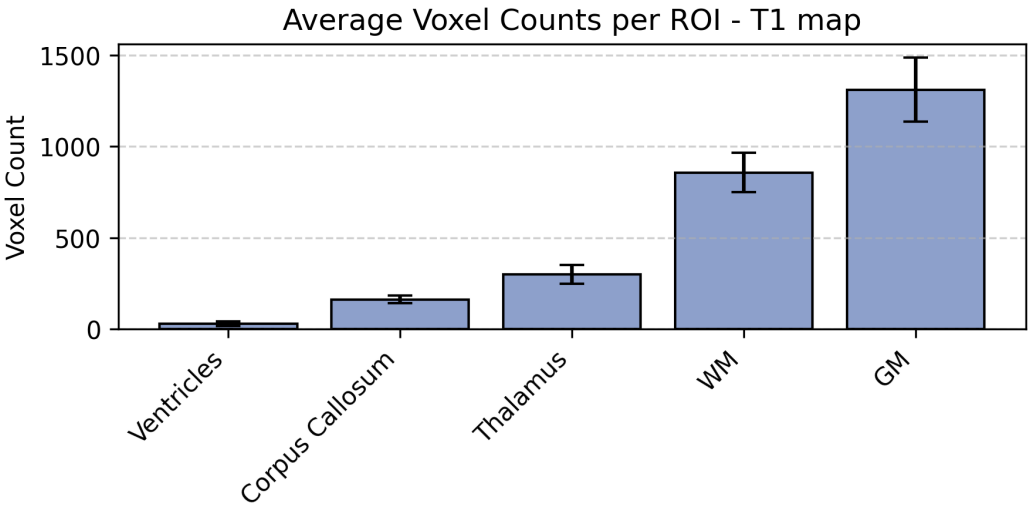

Figure 3.19 Average voxel count for each region of interest in T_1 maps.

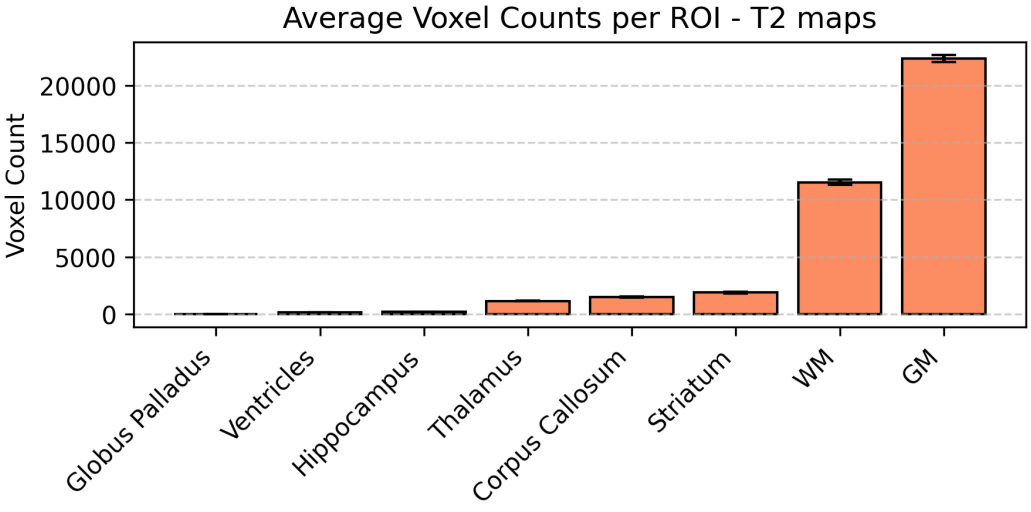

Figure 3.20 Average voxel count for each region of interest in T_2 maps.

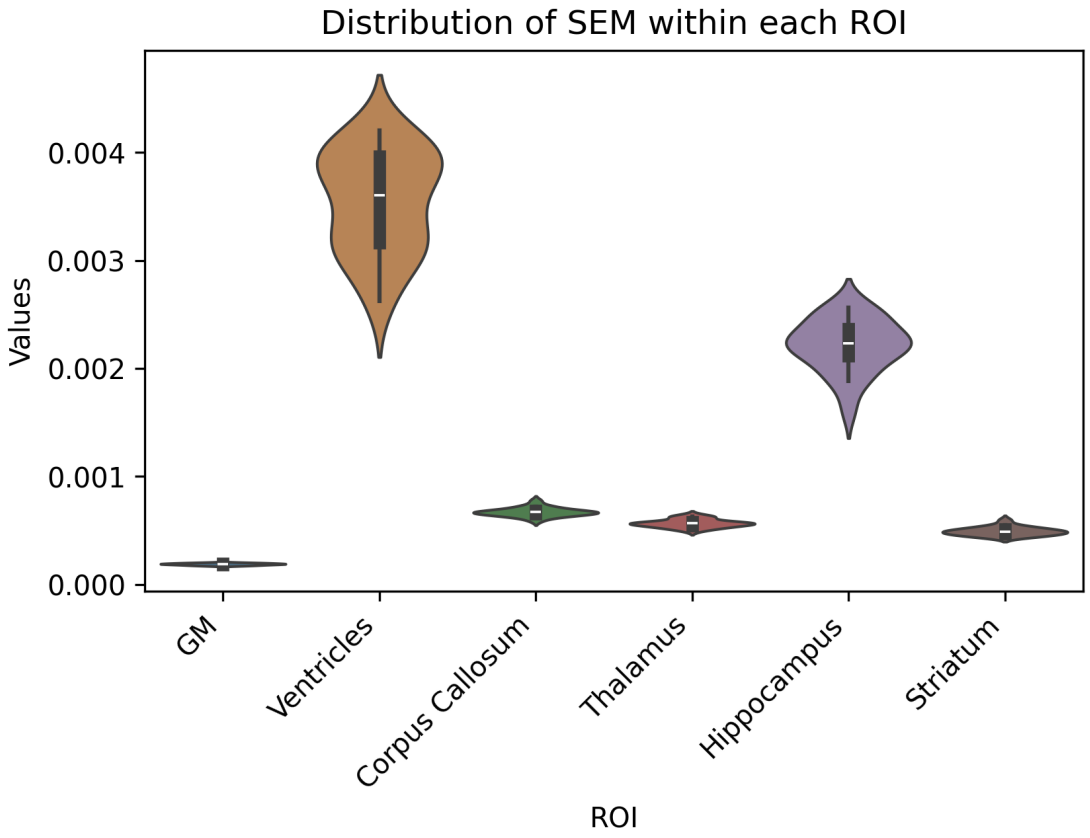

Figure 3.21 Distribution of SEM of susceptibility values for each ROI using all subjects' data. White matter is not shown because it is the reference value, and globus pallidus was omitted because its distribution was much larger that other regions were not visible.

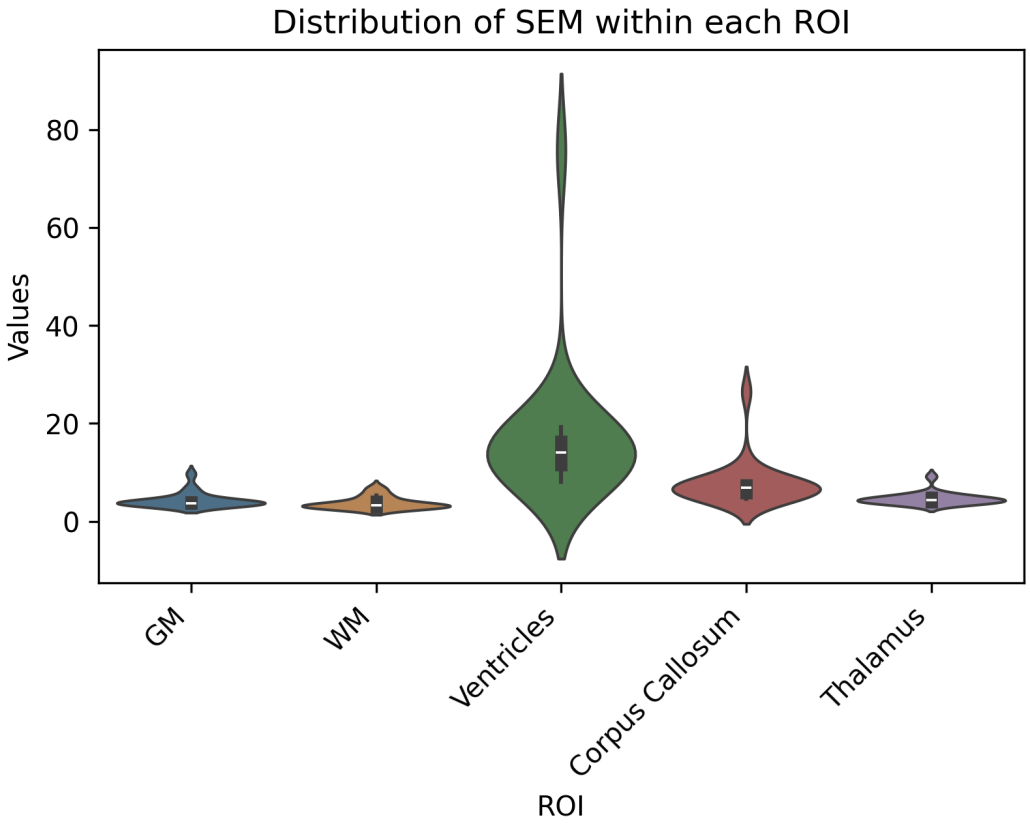

Figure 3.22 Distribution of SEM of T_1 relaxation time values for each ROI using all subjects' data.

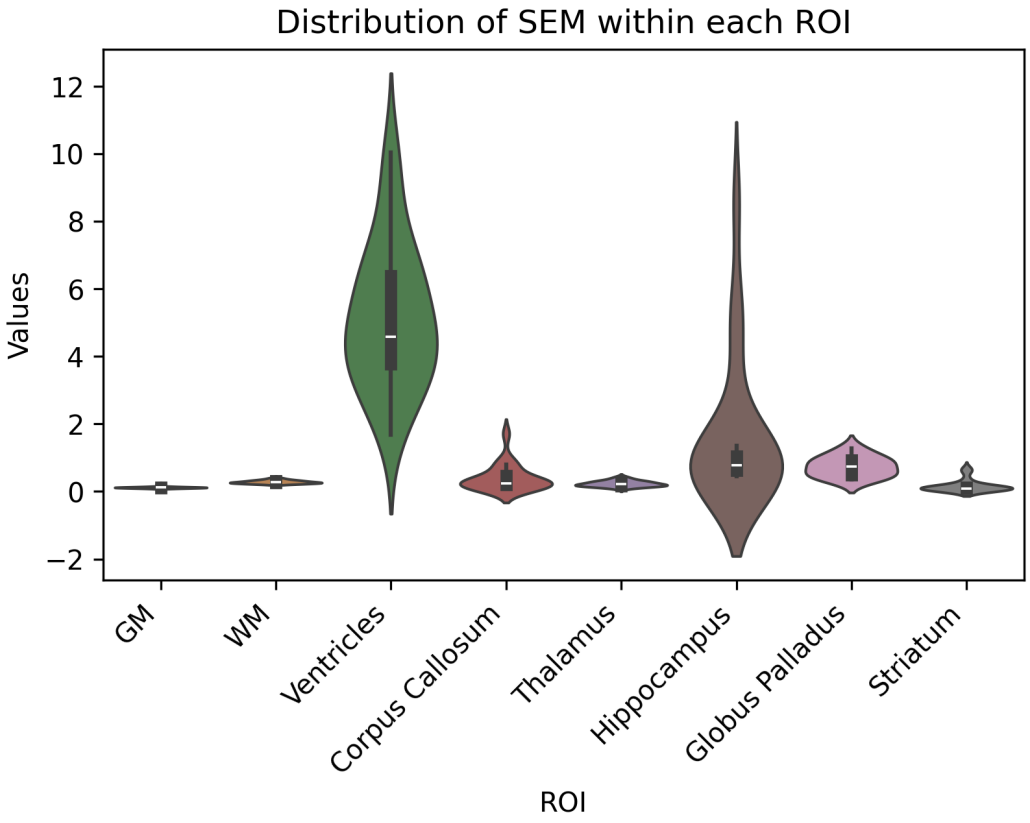

Figure 3.23 Distribution of SEM of T_2 relaxation time values for each ROI using all subjects' data.

4. DISCUSSION

The toolbox produces a fairly BIDS-compliant dataset, and warnings and errors flagged by the validator (refer to Figure 3.2) are results of being a work in progress. The error related to missing echo time and inversion time information in the names of the datasets is because we preferred combining all echos and inversion times into 4D datasets, and correcting the TE and TI information thereafter by injecting the correct values into the Nifti headers and json sidecars. This does not change the fact that the dataset is still not BIDS compliant, and it is possible to modify the code to produce a completely BIDS compliant dataset. All other warnings are because the dataset does not have some of the recommended fields, which are not included because the project is ongoing, therefore information like authors or license are yet to be determined. The GUI satisfies the basic functionality of producing relaxometry images using raw data and masks, and it provides a foundation for further developments like adding visualization, segmentation, and quality control functionalities.

4.1 Validation for the Optimum Pipeline

Table 3.1 shows a clear decrease in computation time and increase in nRMSE score as the value of ε decreases, and one may be tempted to conclude that increasing the threshold will improve the image. However, visual inspection of the resultant map in Figure 3.5 shows severe streaking artifacts, and shows a clear degradation of the map quality as the threshold increases. This is because as the threshold increases, more frequency data is discarded, and consequently the resultant image looks unnatural. For consecutive comparison, the value 0.15 was chosen to compare with other algorithms.

Table 3.2 shows a summary of computation time and nRMSE score for each of the algorithms compared. iLSQR takes more than 1.5 hours -because of the number of iterations used (100)- but doesn't cause substantial improvements in nRMSE and

streaking artifact reduction (as shown in Figure 3.6) compared to TKD. STAR-QSM, on the other hand, has a comparable nRMSE score but a much improved reduction of streaking artifacts, as can be seen in Figure 3.6. As a result, STAR-QSM was preferred for subsequent preprocessing of data.

4.2 Multiparametric Quantitative Maps

The produced T_1 maps show visually good contrast as can be seen in Figure 3.7. The SIGMA atlas was used to segment the T_1 maps from all subjects and calculate the average T_1 relaxation times for the examined regions of interest. Table 3.3 shows average and standard deviation for all maps and regions, and Figure 3.11 shows the distribution of T_1 values for each ROI.

The bias calculated for T_1 maps seems to be quite high (Figure 3.15), but upon revision of qMRLab's MATLAB code, no correction step was found. This could be because the code was not designed for this specific kind of data. So, effectively qMRLab calculates the apparent T_1. Despite the high bias, all regions of interest (ROIs) seem to fall within the acceptable range. This is also applicable for T_2 (Figure 3.16) and R_2^* (Figure 3.17) except that for T_2, GM seems to fall beyond the acceptable range. This is likely because of the chosen algorithm in qMRLab. Fitting after making the problem linear may be faster and computationally less demanding, but it has been shown to yield different measurements compared to the Levenberg-Marquardt algorithm [54]. In any case, this was run as a sanity check, and more data is required to draw a meaningful conclusion based on Bland-Altman analysis.

T_1 values are comparable to those in literature in Table 4.1. Corpus callosum and ventricles showed the highest standard deviation in T_1 maps (Table 3.3) with the smallest number of voxels (Figure 3.19), which causes a noticeable difference in their SEM values compared to other regions (Figure 3.22). Similar patterns are also observed in other maps, likely because ventricles (and other structures for that manner) are small structures and hard to delineate in segmentation, particularly with challenging

resolutions.

A summary of T_2 values in literature is given in Table 4.2. It should be noted that field strength, rat strain, sex, and age of subjects influence T_2 values. Values reported in literature are taken from male Wistar rats [55], Long Evans [56], or Sprague-Dawley [57]. Although all mentioned studies reports using 7T scanners, no age information was given for Long Evans and male Wistar rats, and the closest data in terms of age is that of Sprague-Dawley (68 ± 5 days) [57], and it is possible to see closer T_2 values to those obtained in this analysis. Moreover, as in T_1, some regions have high standard deviation and low voxel count, making their SEM score higher. In any case, relaxometry data have been shown to exhibit slight variance between processing pipelines and data acquisition centers [58].

QSM images show good contrast, and it is possible to see deep brain structures like the striatum. Small structures like the ventricles and globus pallidus become more challenging to trace out as resolution decreases, but at the same time high resolutions require longer scan times and computational power. However, a sweet spot should be determined by extensive experiments and simulations, as low resolutions and limited coverage affect the accuracy of calculated susceptibility values [59] and introduce partial volume effects. Oblique positioning of subjects inside the scanner can also affect susceptibility values in some algorithms, because the direction of the B_0 field is assumed to be along the z-axis in most algorithms [60]. So, a more comprehensive analysis should account for that as well. Another assumption of most algorithms is the isotropy of susceptibility, which was disproved, and the microstructure of white matter was found to make susceptibility anisotropic [11]. Other than STI, COSMOS (Calculation of susceptibility through multiple orientation sampling) uses multiple orientations to reconstruct susceptibility, but also assumes isotropy in each orientation [61]. Another approach that does not assume susceptibility isotropy in single orientation QSM is a recent physics-informed deep learning model called Deepole [27]. It is trained on synthetic data that includes mixtures of random susceptibility sources and tested on the in silico human phantom provided by the QSM Challenge 2.0, showing a promising performance [2]. Many other deep learning models are available in literature, and the

advancements in optimization and validation in human QSM should be extended for preclinical QSM as well.

4.3 Limitations and Future Directions

To enable multiparametric quantitative MRI while keeping the scan time reasonable, trade-offs are made in terms of resolution. Reduced resolution increases partial volume effects, and makes it more challenging to obtain precise measurements. So, more quality control metrics are needed to evaluate images (like the Signal-to-noise ratio (SNR) and Contrast-to-noise ratio (CNR)) to better understand how these parameters influence T_1 and T_2 values. Moreover, it seems important to increase the sample size in Bland-Altman tests.

As for QSM, it is paramount to create and use means for validation and optimization of algorithms for various resolutions in preclinical applications. The phantom introduced in this work is an important yet primitive step that needs further improvements, as piecewise phantoms do not exactly resemble real biological tissue, and do not account for important factors like microstructure. Moreover, it is created based on a post-mortem atlas, which still provides great insight into how the morphology of brain structures impact the preprocessing steps, but fails to answer questions about in-vivo factors like the impact of blood flow and CSF. Furthermore, other methods like deep learning should be tested and compared against other classical methods, thus contributing to establishing a foundation for the standardization of QSM preprocessing and analysis in preclinical applications.

Table 4.1
T_1 values for different ROIs from literature. Am, amygdala; Au1, primary auditory cortex; CC, corpus callosum; Cpu, caudate putamen; DLG, dorsolateral geniculate nucleus; H, hippocampus; M1, primary motor cortex; S1BF, primary somatosensory cortex, barrel field; V1B, primary visual cortex; V2L, secondary visual cortex, lateral area; SD, Sprague-Dawley; LE, Long Evans.

ROI	Value (ms) (mean ± standard deviation)	Rat strain	Reference
Thalamus	1600	SD-Male	[58]
3^{rd} and 4^{th} ventricles	1900	SD-Male	[58]
Lateral ventricle	1950	SD-Male	[58]
Cerebellum	1800	SD-Male	[58]
Cerebellar white matter	1650	SD-Male	[58]
Cortical white matter	1700	SD-Male	[58]
Cingulate cortex	1890	SD-Male	[58]
Frontal cortex	1880	SD-Male	[58]
Olfactory bulb	1840	SD-Male	[58]
Parietal cortex	1795	SD-Male	[58]
Temporal cortex	1905	SD-Male	[58]
Trigeminal nerve	1328 ± 63	SD-Female	[62]
Cortex	1690	SD-Female	[62]
Cpu	1610	SD-Female	[62]
Am	2050 ± 30	LE Male	[56]
Au1	1930 ± 60	LE Male	[56]
DLG	1630 ± 10	LE Male	[56]
H	2050 ± 60	LE Male	[56]
M1	2000 ± 30	LE Male	[56]
S1BF	1920 ± 40	LE Male	[56]
V1B	1980 ± 40	LE Male	[56]
V2L	2200 ± 40	LE Male	[56]
CC	1510 ± 80	LE Male	[56]

Table 4.2
In vivo T_2 relaxation times for specific brain areas in the rat from three studies. Am, amygdala; Au1, primary auditory cortex; CC, corpus callosum; Cpu, caudate putamen; DLG, dorsolateral geniculate nucleus; H, hippocampus; M1, primary motor cortex; S1BF, primary somatosensory cortex, barrel field; V1B, primary visual cortex; V2L, secondary visual cortex, lateral area.

Structure	T_2 (ms) [56]	T_2 (ms) [55]	T_2 (ms) [57]
Am	53.1 ± 0.9	-	61.20 ± 1.41
Au1	49.1 ± 0.6	-	-
CC	39.8 ± 0.7	35.8 ± 1.8	-
Cpu	48.4 ± 0.6	42.1 ± 1.5	54.89 ± 0.75
DLG	42.9 ± 0.4	-	-
H	51.4 ± 0.6	47.9 ± 0.6	58.33 ± 1.07
M1	50.7 ± 0.6	-	-
S1BF	48.2 ± 0.6	-	-
V1B	48.6 ± 0.5	-	-
V2L	50.4 ± 0.3	-	-
Cortex	-	41.8 ± 1.7	56.80 ± 0.75
Striatum	-	-	56.37 ± 1.15
Insular cortex	-	-	59.41 ± 0.92
Thalamus	-	-	52.85 ± 0.80
Hypothalamus	-	-	56.65 ± 1.46
Piriform cortex	-	-	60.95 ± 0.91
White matter	-	-	53.32 ± 0.91

5. CONCLUSION

A multiparametric quantitative MRI pipeline was demonstrated and used on a group of 21 female Wistar rats. It enables BIDS-compliant conversion of the dataset and provides a simple GUI for simple quantitative mapping tasks. As for streamlined relaxometry, it produced acceptable results compared to other toolboxes used in literature. Sample size for Bland-Altman will be increased to yield more statistically powerful conclusions. As for QSM, a phantom was used to choose the best algorithm, which was found to be STAR-QSM. Consecutive preprocessing of data was run using STAR-QSM. Improvement of the phantom is necessary for more sophisticated validation and optimization, especially for in-vivo preclinical applications, and cutting-edge deep learning models will be compared to classical methods including the ones used in this work.

APPENDIX A. DERIVATION OF THE LAPLACIAN-BASED PHASE UNWRAPPING EQUATION

We first review some basic mathematical properties to have them at hand whenever needed.

A.1 Multivariable Chain Rule and Second Derivatives

If f is a function of x ($f(x)$) and x is a function of ϕ ($x(\phi)$), then using the chain rule, the first derivative is:

$$\frac{df}{d\phi} = \frac{df}{dx}\frac{dx}{d\phi} \tag{A.1}$$

To find the second derivative, the chain rule can be used again together with the product rule:

$$\begin{aligned}
\frac{d^2f}{d\phi^2} &= \frac{d}{d\phi}\left(\frac{df}{dx}\frac{dx}{d\phi}\right) \\
&= \frac{d}{d\phi}\left(\frac{df}{dx}\right)\frac{dx}{d\phi} + \frac{d}{d\phi}\left(\frac{dx}{d\phi}\right)\frac{df}{dx} \\
&= \frac{d^2f}{dx^2}\frac{dx}{d\phi}\frac{dx}{d\phi} + \frac{d^2x}{d\phi^2}\frac{df}{dx} \\
&= \frac{d^2f}{dx^2}\left(\frac{dx}{d\phi}\right)^2 + \frac{d^2x}{d\phi^2}\frac{df}{dx} \\
\Rightarrow \frac{d^2f}{d\phi^2} &= \frac{d^2f}{dx^2}\left(\frac{dx}{d\phi}\right)^2 + \frac{d^2x}{d\phi^2}\frac{df}{dx}
\end{aligned} \tag{A.2}$$

A.2 Applying the Laplacian

The Laplacian operator is defined as [63]:

$$\nabla^2 = \left(\frac{\partial^2}{\partial x^2}, \frac{\partial^2}{\partial y^2}, \frac{\partial^2}{\partial z^2}\right) \tag{A.3}$$

Let ϕ and ψ be the unwrapped and wrapped phases, respectively. We can then use Euler's formula:

$$\begin{aligned} e^{i\phi} &= \cos(\phi) + i\sin(\phi) \\ \Rightarrow \nabla^2 e^{i\phi} &= \nabla^2\left(\cos(\phi) + i\sin(\phi)\right) \\ \text{But since } \nabla^2 \text{ is linear :} & \\ \nabla^2 e^{i\phi} &= \nabla^2\cos(\phi) + \nabla^2 i\sin(\phi) \\ \text{For the real part (using Eq. A.2):} & \\ \nabla^2\cos(\phi) &= -\cos(\phi)\left(\nabla\phi\right)^2 - \sin(\phi)\nabla^2\phi \\ \text{For the imaginary part (using Eq. A.2):} & \\ \nabla^2\sin(\phi) &= -\sin\phi\left(\nabla\phi\right)^2 + \cos(\phi)\nabla^2\phi \end{aligned} \tag{A.4}$$

Since $\nabla\phi$ is tiny, it can be ignored. Therefore:

$$\begin{aligned} \Im\left(\nabla^2 e^{i\phi}\right) &\approx \cos(\phi)\nabla^2\phi \\ \Rightarrow \nabla^2\phi &\approx \frac{\Im\left(\nabla^2 e^{i\phi}\right)}{\cos(\phi)} \end{aligned} \tag{A.5}$$

But since

$$\phi = \psi + 2\pi k \mid k \in \mathbb{Z}$$

We can exchange ϕ with ψ in trigonometric expressions

$$\begin{aligned} \Rightarrow e^{i\phi} &= e^{i\psi} \\ \Rightarrow \cos(\phi) + i\sin(\phi) &= \cos(\psi) + i\sin(\psi) \\ \Rightarrow \nabla^2\cos(\phi) + \nabla^2 i\sin(\phi) &= \nabla^2\cos(\psi) + \nabla^2 i\sin(\psi) \\ \Rightarrow \Im\left(\nabla^2 e^{i\phi}\right) &= \Im\left(\nabla^2 e^{i\psi}\right) = \nabla^2\sin(\psi) \; and \; \cos(\phi) = \cos(\psi) \end{aligned} \tag{A.6}$$

Combining A.5 and A.6:

$$\begin{aligned} \nabla^2\phi &\approx \frac{\nabla^2 \sin(\psi)}{\cos(\psi)} \\ \Rightarrow \cos(\psi)\nabla^2\phi &\approx \nabla^2 \sin(\psi) \end{aligned} \tag{A.7}$$

The same can be done with $\Re\left(\nabla^2 e^{i\phi}\right)$, after also neglecting $\nabla\phi$ because it is very small:

$$\begin{aligned} \Re\left(\nabla^2 e^{i\phi}\right) &\approx -\sin(\phi)\nabla^2\phi \\ \Rightarrow \nabla^2\phi &\approx -\frac{\Re\left(\nabla^2 e^{i\phi}\right)}{\sin(\phi)} \\ &\approx -\frac{\Re\left(\nabla^2 e^{i\psi}\right)}{\sin(\psi)} \\ &\approx -\frac{\nabla^2 \cos(\psi)}{\sin(\psi)} \\ \Rightarrow \sin(\psi)\nabla^2\phi &\approx -\nabla^2 \cos(\psi) \end{aligned} \tag{A.8}$$

Using both A.7 and A.8:

$$\sin(\psi)\nabla^2\phi \approx -\nabla^2 \cos(\psi)$$

Multiplication by $\sin(\psi)$ yields:

$$\sin^2(\psi)\nabla^2\phi \approx -\nabla^2 \cos(\psi)\sin(\psi)$$

Similarly:

$$\cos(\psi)\nabla^2\phi \approx \nabla^2 \sin(\psi)$$

Multiplication by $\cos(\psi)$ yields:

$$\cos^2(\psi)\nabla^2\phi \approx \nabla^2 \sin(\psi)\cos(\psi) \tag{A.9}$$

Summing both parts yields:

$$\begin{aligned} \left(\cos^2(\psi) + \sin^2(\psi)\right)\nabla^2\phi &\approx \nabla^2 \sin(\psi)\cos(\psi) - \nabla^2 \cos(\psi)\sin(\psi) \\ \Rightarrow \nabla^2\phi &\approx \nabla^2 \sin(\psi)\cos(\psi) - \nabla^2 \cos(\psi)\sin(\psi) \\ \Rightarrow \boxed{\phi \approx \frac{\nabla^2 \sin(\psi)\cos(\psi) - \nabla^2 \cos(\psi)\sin(\psi)}{\nabla^2}} \end{aligned}$$

Division by the Laplacian operator is possible in the Fourier space, thus enabling calculation of unwrapped phase given wrapped phase.

APPENDIX B. BACKGROUND FIELD REMOVAL

The total field image obtained after phase unwrapping represents the total perturbation from the magnetic field, which is affected by sources outside the region of interest (ROI - brain in this case). These large susceptibility effects from outside the brain propagate into the ROI, and it is a few orders larger than those within the brain. For example, air has a susceptibility value of 9 ppm, whereas that of brain tissue is on the order of 0.01-0.05 ppm [3]. This makes it quite hard to estimate the correct values of susceptibility inside the ROI. Multiple approaches have been adapted in literature to minimize the effect of these sources, including projection onto dipole field (PDF) [19] and sophisticated harmonic artifact reduction for phase data (SHARP) [64]. Some approaches combine both phase unwrapping and background field removal [65], and many deep learning approaches have emerged for this purpose [66, 67]. SHARP is adapted in this work with its various variations. The assumption is that the total field has multiple components: the underlying tissue field (internal field) and the static magnetic field [20]. This can be mathematically expressed as:

$$\vec{B}_{tot} = \vec{B}_{int} + \vec{B}_{background} \tag{B.1}$$

Susceptibility is related to the internal field by [64]:

$$B_{int}(\vec{r}) = B_0 \int_{VOI} \chi\left(\vec{r}\right) d_z \left(\vec{r} - \vec{r'}\right) d^3\vec{r'} \tag{B.2}$$

So, we are interested in $\vec{B}_{int}$. Since $\vec{B}_{background}$ originates outside the brain, its component is harmonic all over the image. Therefore, it is possible to utilize the mean value property of harmonic functions to extract the relevant information.

B.1 Sophisticated Harmonic Artifact Reduction for Phase Data (SHARP)

The background field is harmonic, therefore, Eq. B.1 can be written as [20]:

$$\begin{aligned} \nabla^2 \vec{B}_{tot} &= \nabla^2 \left(\vec{B}_{int} + \vec{B}_{background} \right) \\ \nabla^2 \vec{B}_{tot} &= \nabla^2 \vec{B}_{int} + \nabla^2 \vec{B}_{background} \end{aligned}$$

Since $\vec{B}_{background}$ is harmonic: (B.3)

$$\begin{aligned} \nabla^2 \vec{B}_{background} &= 0 \\ \Rightarrow \nabla^2 \vec{B}_{tot} &= \nabla^2 \vec{B}_{int} \end{aligned}$$

Solving this differential equation is possible using the mean value theorem property. According to the mean value theorem, a harmonic function is not changed by convolution with a nonnegative, radially symmetric, normalized kernel. Applying this property:

$$\begin{aligned} \vec{B}_{interim} &= \vec{B}_{total} - \rho \otimes \vec{B}_{total} \\ \vec{B}_{interim} &= \vec{B}_{int} + \vec{B}_{background} - \rho \otimes \vec{B}_{int} - \rho \otimes \vec{B}_{background} \\ \vec{B}_{interim} &= \vec{B}_{int} - \rho \otimes \vec{B}_{int} \\ \vec{B}_{interim} &= (\delta - \rho) \otimes \vec{B}_{int} \end{aligned} \tag{B.4}$$

Where δ is the impulse function, ρ is the radial function, and $\otimes$ is the convolution operator. This means that $\vec{B}_{int}$ can be obtained using deconvolution ($\otimes^{-1}$):

$$\boxed{\vec{B}_{int} = (\delta - \rho) \otimes^{-1} \vec{B}_{interim}} \tag{B.5}$$

which is applied after $B_{interim}$ is the masked with the brain mask. In v-SHARP, $B_{interim}$ is iteratively constructed with different erosion amounts that depend on the radius of the spherical kernel used.

APPENDIX C. DIPOLE INVERSION FOR SUSCEPTIBILITY ESTIMATION

When a sample with a magnetic susceptibility distribution $\chi(\boldsymbol{r})$ is placed in an external magnetic field (B_0), oriented along the z-axis, the z-component of the induced magnetization becomes nonzero and is given by

$$M_z(\boldsymbol{r}) = \chi(\boldsymbol{r})\frac{B_0}{\mu_0\mu_r(\boldsymbol{r})} = \chi(\boldsymbol{r})\frac{B_0}{\mu_0(1+\chi(\boldsymbol{r}))} \approx \chi(\boldsymbol{r})\frac{B_0}{\mu_0} \tag{C.1}$$

where it is assumed that $\chi \ll 1$. The magnetic field induced at a location $\boldsymbol{r}$ by the resulting magnetization distribution is described as

$$\boldsymbol{B}_d(\boldsymbol{r}) = \frac{\mu_0}{4\pi}\int \frac{1}{|\boldsymbol{r}-\boldsymbol{r'}|^3} \times \left(3\frac{\boldsymbol{M}(\boldsymbol{r'}).(\boldsymbol{r}-\boldsymbol{r'})}{|\boldsymbol{r}-\boldsymbol{r'}|^2}(\boldsymbol{r}-\boldsymbol{r'}) - \boldsymbol{M}(\boldsymbol{r'})\right) d^3\boldsymbol{r'} \tag{C.2}$$

where $\boldsymbol{M}(\boldsymbol{r'})$ represents elements of the magnetization distribution. This is a complex and nonlocal expression, and it can be made simpler and local when calculated in the Fourier domain [68]:

$$\tilde{\boldsymbol{B}}_d(\boldsymbol{k}) = \frac{\mu_0}{3}\frac{\cos^2\beta - 1}{2}(\tilde{\boldsymbol{M}}(\boldsymbol{k}) - 3\tilde{M}_z(\boldsymbol{k})\hat{\boldsymbol{z}}) \tag{C.3}$$

where $\boldsymbol{k}$ is the coordinate position in k-space, $\tilde{M}(\boldsymbol{k})$ and $\tilde{M}_z(\boldsymbol{k})$ are the three dimensional Fourier transforms of $\boldsymbol{M}(\boldsymbol{r})$ and $M_z(\boldsymbol{r})$, $\hat{z}$ is a unit vector in the z-direction, while β is the angle between the direction of the main magnetic field and $\boldsymbol{k}$ such that

$$C = 3\cos^2\beta - 1 = 3\frac{k_z^2}{k_x^2+k_y^2+k_z^2} - 1 \tag{C.4}$$

This is later used in deconvolution, which is division in the Fourier space, to get susceptibility. But there are values where this expression equals zero, thus making conversion ill-posed. The angle at which this statement is nullified ($\beta = 54.7°$) creates a zero-cone. Many methods are suggested to solve this ill-posed problem. One of the initial attempts was threshold based k-space division, which was described previously.

C.1 LSQR

$$\psi(\boldsymbol{k}) = D_2(\boldsymbol{k}).\chi(\boldsymbol{k}) \tag{C.5}$$

where $\psi(\boldsymbol{k})$ and $\chi(\boldsymbol{k})$ are the Fourier transforms of $\psi(\boldsymbol{r})$ (local phase) and $\chi(\boldsymbol{r})$ (susceptibility). Moreover,

$$D_2(\boldsymbol{k}) = \frac{1}{3} - \frac{k_z^2}{k_x^2 + k_y^2 + k_z^2} \tag{C.6}$$

Taking the derivative of the this expression with respect to k_z:

$$\begin{aligned} \frac{\partial \psi(\boldsymbol{k})}{\partial k_z} &= \frac{\partial \left(D_2(\boldsymbol{k}).\chi(\boldsymbol{k})\right)}{\partial k_z} \\ \psi'(\boldsymbol{k}) &= D_2'(\boldsymbol{k}).\chi(\boldsymbol{k}) + \chi'(\boldsymbol{k}).D_2(\boldsymbol{k}) \end{aligned} \tag{C.7}$$

calculating $D_2'(\boldsymbol{k})$ first:

$$\begin{aligned} D_2'(\boldsymbol{k}) &= \frac{\partial}{\partial k_z}\left(\frac{1}{3} - \frac{k_z^2}{k_x^2 + k_y^2 + k_z^2}\right) \\ &= \frac{-2k_z\left(k_x^2 + k_y^2 + k_z^2\right) + 2k_z(k_z^2)}{\left(k_x^2 + k_y^2 + k_z^2\right)^2} \\ &= \boxed{\frac{-2k_z(k_x^2 + k_y^2)}{\left(k_x^2 + k_y^2 + k_z^2\right)^2}} \end{aligned} \tag{C.8}$$

defining another kernel for brevity:

$$D_2'(\boldsymbol{k}) = -\frac{2k_z\left(k_x^2 + k_y^2\right)}{\left(k_x^2 + k_y^2 + k_z^2\right)^2} \quad =: D_3(\boldsymbol{k}). \tag{C.9}$$

Eq. C.7 becomes

$$\psi'(\boldsymbol{k}) \;=\; D_3(\boldsymbol{k})\,\chi(\boldsymbol{k}) \;+\; D_2(\boldsymbol{k})\,\chi'(\boldsymbol{k}). \tag{C.10}$$

Using the Fourier derivative identities, it is possible to find $\psi'(\boldsymbol{k})$ and $\chi'(\boldsymbol{k})$:

$$\psi'(\boldsymbol{k}) = \mathcal{F}\{-i2\pi r_z\,\psi(\boldsymbol{r})\}\,(\boldsymbol{k}), \qquad \chi'(\boldsymbol{k}) = \mathcal{F}\{-i2\pi r_z\,\chi(\boldsymbol{r})\}\,(\boldsymbol{k}). \tag{C.11}$$

Eq. C.10 becomes

$$D_3(\boldsymbol{k})\,\chi(\boldsymbol{k}) \;+\; D_2(\boldsymbol{k})\,\mathcal{F}\{-i2\pi r_z\,\chi(\boldsymbol{r})\}\,(\boldsymbol{k}) \;=\; \mathcal{F}\{-i2\pi r_z\,\psi(\boldsymbol{r})\}\,(\boldsymbol{k}). \tag{C.12}$$

Near the conical surface where $D_2(\boldsymbol{k}) \approx 0$, the second term is negligible, so

$$\boxed{\chi(\boldsymbol{k}) \;\approx\; \frac{\mathcal{F}\{-i2\pi r_z\,\psi(\boldsymbol{r})\}\,(\boldsymbol{k})}{D_3(\boldsymbol{k})} \quad \text{(on/near the cone)}} \tag{C.13}$$

Away from the cone ($|D_2(\boldsymbol{k})| \geq \varepsilon$),

$$\boxed{\chi(\boldsymbol{k}) \;=\; \frac{\psi(\boldsymbol{k})}{D_2(\boldsymbol{k})} \quad (\text{for } |D_2| \geq \varepsilon)} \tag{C.14}$$

Putting these together, a practical piecewise inversion is

$$\chi(\boldsymbol{k}) \;=\; \begin{cases} \dfrac{\psi(\boldsymbol{k})}{D_2(\boldsymbol{k})}, & |D_2(\boldsymbol{k})| \geq \varepsilon, \\ \dfrac{\mathcal{F}\{-i2\pi r_z\,\psi(\boldsymbol{r})\}\,(\boldsymbol{k})}{D_3(\boldsymbol{k})}, & |D_2(\boldsymbol{k})| < \varepsilon. \end{cases} \tag{C.15}$$

REFERENCES

1. Haacke, E. M., and J. R. Reichenbach, *Susceptibility Weighted Imaging in MRI: Basic Concepts and Clinical Applications*, Wiley-Blackwell, 2011.

2. Marques, J. J., "Quantitative susceptibility mapping (QSM) challenge 2.0."

3. Schweser, F., A. Deistung, and J. R. Reichenbach, "Foundations of MRI phase imaging and processing for Quantitative Susceptibility Mapping (QSM)," *Zeitschrift für Medizinische Physik*, Vol. 26, no. 1, pp. 6–34, 2016.

4. Liu, C., W. Li, K. A. Tong, K. W. Yeom, *et al.*, "Susceptibility-Weighted Imaging and Quantitative Susceptibility Mapping in the Brain," *Journal of Magnetic Resonance Imaging : JMRI*, Vol. 42, no. 1, pp. 23–41, 2015.

5. Kabasawa, H., "MR Imaging in the 21st Century: Technical Innovation over the First Two Decades," *Magnetic Resonance in Medical Sciences*, Vol. 21, no. 1, pp. 71–82, 2021.

6. Grover, V. P., J. M. Tognarelli, M. M. Crossey, I. J. Cox, *et al.*, "Magnetic Resonance Imaging: Principles and Techniques: Lessons for Clinicians," *Journal of Clinical and Experimental Hepatology*, Vol. 5, no. 3, pp. 246–255, 2015.

7. Liang, Z.-P., and P. C. Lauterbur, *Principles of Magnetic Resonance Imaging: A Signal Processing Perspective*, Wiley-IEEE Press, 2000.

8. Cercignani, M., N. G. Dowell, and P. S. Tofts, *Quantitative MRI of the Brain: Principles of Physical Measurement*, CRC Press, 2 ed., 2018.

9. Bloch, F., "Nuclear Induction," *Physical Review*, Vol. 70, no. 7–8, pp. 460–474, 1946.

10. "The Nobel Prize in Physics 1952."

11. Wharton, S., and R. Bowtell, "Effects of white matter microstructure on phase and susceptibility maps," *Magnetic Resonance in Medicine*, Vol. 73, no. 3, pp. 1258–1269, 2015.

12. Gozt, A., S. Hellewell, P. G. D. Ward, M. Bynevelt, *et al.*, "Emerging Applications for Quantitative Susceptibility Mapping in the Detection of Traumatic Brain Injury Pathology," *Neuroscience*, Vol. 467, pp. 218–236, 2021.

13. Yan, F., N. He, and E. M. Haacke, "Editorial: Quantitative Susceptibility Mapping in Neurodegeneration," *Frontiers in Neuroscience*, Vol. 15, p. 724550, 2021.

14. Duan, X., Y. Xie, X. Zhu, L. Chen, *et al.*, "Quantitative Susceptibility Mapping of Brain Iron Deposition in Patients With Recurrent Depression," *Psychiatry Investigation*, Vol. 19, no. 8, pp. 668–675, 2022.

15. Garcia Sabori, M., A. Jara, N. Munoz, C. Milovic, *et al.*, "Quantitative Susceptibility Mapping MRI in Deep-Brain Nuclei in First-Episode Psychosis," *Schizophrenia Bulletin*, Vol. 49, no. 5, pp. 1355–1363, 2023.

16. Qin, Z., W. Wu, D. Liu, C. Zheng, *et al.*, "Quantitative Susceptibility Mapping of Brain Iron Relating to Cognitive Impairment in Hypertension," *Journal of Magnetic Resonance Imaging*, Vol. 56, no. 2, pp. 508–515, 2022.

17. Tang, S., Y. Xu, X. Liu, Z. Chen, *et al.*, "Quantitative susceptibility mapping shows lower brain iron content in children with autism," *European Radiology*, Vol. 31, no. 4, pp. 2073–2083, 2021.

18. Tang, S., G. Zhang, Q. Ran, L. Nie, *et al.*, "Quantitative susceptibility mapping shows lower brain iron content in children with attention-deficit hyperactivity disorder," *Human Brain Mapping*, Vol. 43, no. 8, pp. 2495–2502, 2022.

19. Liu, T., I. Khalidov, L. d. Rochefort, P. Spincemaille, *et al.*, "A novel background field removal method for MRI using projection onto dipole fields (PDF)," *NMR in Biomedicine*, Vol. 24, no. 9, pp. 1129–1136, 2011.

20. Li, L., and J. S. Leigh, "High-Precision Mapping of the Magnetic Field Utilizing the Harmonic Function Mean Value Property," *Journal of Magnetic Resonance*, Vol. 148, no. 2, pp. 442–448, 2001.

21. Jung, W., S. Bollmann, and J. Lee, "Overview of quantitative susceptibility mapping using deep learning: Current status, challenges and opportunities," *NMR in Biomedicine*, Vol. 35, no. 4, p. e4292, 2022.

22. Özbay, P. S., A. Deistung, X. Feng, D. Nanz, *et al.*, "A comprehensive numerical analysis of background phase correction with V-SHARP," *NMR in Biomedicine*, Vol. 30, no. 4, 2017.

23. Wharton, S., A. Schäfer, and R. Bowtell, "Susceptibility mapping in the human brain using threshold-based k-space division," *Magnetic Resonance in Medicine*, Vol. 63, no. 5, pp. 1292–1304, 2010.

24. Li, W., B. Wu, and C. Liu, "Quantitative susceptibility mapping of human brain reflects spatial variation in tissue composition," *NeuroImage*, Vol. 55, no. 4, pp. 1645–1656, 2011.

25. Paige, C. C., and M. A. Saunders, "LSQR: An Algorithm for Sparse Linear Equations and Sparse Least Squares," *ACM Transactions on Mathematical Software*, Vol. 8, no. 1, pp. 43–71, 1982.

26. Wei, H., R. Dibb, Y. Zhou, Y. Sun, *et al.*, "Streaking Artifact Reduction for Quantitative Susceptibility Mapping of Sources with Large Dynamic Range," *NMR in Biomedicine*, Vol. 28, no. 10, p. 1294, 2015.

27. Jochmann, T., F. Salman, M. G. Dwyer, N. Bergsland, *et al.*, "Quantitative susceptibility mapping in magnetically inhomogeneous tissues," *Magnetic Resonance in Medicine*, Vol. 94, no. 3, pp. 1044–1059, 2025.

28. Hamezah, H. S., L. W. Durani, N. F. Ibrahim, D. Yanagisawa, *et al.*, "Volumetric changes in the aging rat brain and its impact on cognitive and locomotor functions," *Experimental Gerontology*, Vol. 99, pp. 69–79, 2017.

29. Gull, S., C. Gaser, K.-H. Herrmann, A. Urbach, *et al.*, "Brain Macro-Structural Alterations in Aging Rats: A Longitudinal Lifetime Approach," *Cells*, Vol. 12, no. 3, p. 432, 2023.

30. Driscoll, I., S. R. Howard, J. C. Stone, M. H. Monfils, *et al.*, "The aging hippocampus: A multi-level analysis in the rat," *Neuroscience*, Vol. 139, no. 4, pp. 1173–1185, 2006.

31. Seiler, A., S. Schöngrundner, B. Stock, U. Nöth, *et al.*, "Cortical aging - new insights with multiparametric quantitative MRI," *Aging (Albany NY)*, Vol. 12, no. 16, p. 16195, 2020.

32. Kupeli, A., M. Kocak, M. Goktepeli, E. Karavas, *et al.*, "Role of T1 mapping to evaluate brain aging in a healthy population," *Clinical Imaging*, Vol. 59, no. 1, pp. 56–60, 2020.

33. Keuken, M. C., P.-L. Bazin, K. Backhouse, S. Beekhuizen, *et al.*, "Effects of aging on T_1, T_2^*, and QSM MRI values in the subcortex," *Brain Structure & Function*, Vol. 222, no. 6, p. 2487, 2017.

34. Kumar, R., S. Delshad, P. M. Macey, M. A. Woo, *et al.*, "Development of T2-relaxation Values in Regional Brain Sites during Adolescence," *Magnetic Resonance Imaging*, Vol. 29, no. 2, pp. 185–193, 2011.

35. Aktaş Dinçer, H., A. M. Ağlıdere, and D. Gökçay, "T1 relaxation time is prolonged in healthy aging: A whole brain study," *Turkish Journal of Medical Sciences*, Vol. 53, no. 3, pp. 675–684, 2023.

36. Bilgic, B., A. Pfefferbaum, T. Rohlfing, E. V. Sullivan, *et al.*, "MRI estimates of brain iron concentration in normal aging using quantitative susceptibility mapping," *NeuroImage*, Vol. 59, no. 3, pp. 2625–2635, 2012.

37. Betts, M. J., J. Acosta-Cabronero, A. Cardenas-Blanco, P. J. Nestor, *et al.*, "High-resolution characterisation of the aging brain using simultaneous quantitative susceptibility mapping (QSM) and R2* measurements at 7T," *NeuroImage*, Vol. 138, pp. 43–63, 2016.

38. Mahmoudi, N., M. Dadak, P. Bronzlik, A. A. Maudsley, *et al.*, "Microstructural and Metabolic Changes in Normal Aging Human Brain Studied with Combined Whole-Brain MR Spectroscopic Imaging and Quantitative MR Imaging," *Clinical Neuroradiology*, Vol. 33, no. 4, pp. 993–1005, 2023.

39. Almeida, A. J. D., B. A. Hobson, N. Saito, D. A. Bruun, *et al.*, "Quantitative T2 mapping-based longitudinal assessment of brain injury and therapeutic rescue in the rat following acute organophosphate intoxication," *Neuropharmacology*, Vol. 249, p. 109895, 2024.

40. Klohs, J., I. W. Politano, A. Deistung, J. Grandjean, *et al.*, "Longitudinal Assessment of Amyloid Pathology in Transgenic *ArcAβ* Mice Using Multi-Parametric Magnetic Resonance Imaging," *PLOS ONE*, Vol. 8, no. 6, p. e66097, 2013.

41. Gigliucci, V., S. Gormley, S. Gibney, J. Rouine, *et al.*, "Characterisation of the antidepressant properties of nitric oxide synthase inhibitors in the olfactory bulbectomised rat model of depression," *European Neuropsychopharmacology*, Vol. 24, no. 8, pp. 1349–1361, 2014.

42. Koundal, S., S. Gandhi, T. Kaur, R. Trivedi, *et al.*, "Investigation of prolonged hypobaric hypoxia-induced change in rat brain using T2 relaxometry and diffusion tensor imaging at 7T," *Neuroscience*, Vol. 289, pp. 106–113, 2015.

43. Del Bigio, M. R., I. Slobodian, A. E. Schellenberg, R. J. Buist, *et al.*, "Magnetic resonance imaging indicators of blood-brain barrier and brain water changes in young rats with kaolin-induced hydrocephalus," *Fluids and Barriers of the CNS*, Vol. 8, no. 1, p. 22, 2011.

44. Barbier, E. L., L. Liu, E. Grillon, J.-F. Payen, *et al.*, "Focal brain ischemia in rat: Acute changes in brain tissue T1 reflect acute increase in brain tissue water content," *NMR in Biomedicine*, Vol. 18, no. 8, pp. 499–506, 2005.

45. Chan, K.-S., and J. P. Marques, "SEPIA-Susceptibility mapping pipeline tool for phase images," *NeuroImage*, Vol. 227, p. 117611, 2021.

46. Yushkevich, P. A., J. Piven, H. C. Hazlett, R. G. Smith, *et al.*, "User-guided 3D active contour segmentation of anatomical structures: Significantly improved efficiency and reliability," *NeuroImage*, Vol. 31, no. 3, pp. 1116–1128, 2006.

47. Tustison, N. J., P. A. Cook, A. J. Holbrook, H. J. Johnson, *et al.*, "The ANTsX ecosystem for quantitative biological and medical imaging," *Scientific Reports*, Vol. 11, no. 1, p. 9068, 2021.

48. Brett, M., C. J. Markiewicz, M. Hanke, M.-A. Cote, *et al.*, "Nipy/nibabel: 5.3.1."

49. Oliver-Taylor, A., A. Li, A. Thomas, A. Flinker, *et al.*, "The brain imaging data structure (BIDS) specification."

50. Deichmann, R., and A. Haase, "Quantification of T1 values by SNAPSHOT-FLASH NMR imaging," *Journal of Magnetic Resonance (1969)*, Vol. 96, no. 3, pp. 608–612, 1992.

51. Barral, J. K., E. Gudmundson, N. Stikov, M. Etezadi-Amoli, *et al.*, "A robust methodology for in vivo T1 mapping," *Magnetic Resonance in Medicine*, Vol. 64, no. 4, pp. 1057–1067, 2010.

52. Johnson, G. A., R. Laoprasert, R. J. Anderson, G. Cofer, *et al.*, "A multicontrast MR atlas of the Wistar rat brain," *NeuroImage*, Vol. 242, p. 118470, 2011.

53. Özbay, P. S., C. Rossi, R. Kocian, M. Redle, *et al.*, "Effect of respiratory hyperoxic challenge on magnetic susceptibility in human brain assessed by quantitative susceptibility mapping (QSM)," *NMR in Biomedicine*, Vol. 28, no. 12, pp. 1688–1696, 2015.

54. Pei, M., T. D. Nguyen, N. D. Thimmappa, C. Salustri, *et al.*, "An Algorithm for Fast Mono-exponential Fitting Based on Auto-Regression on Linear Operations (ARLO) of Data," *Magnetic Resonance in Medicine : Official Journal of the Society of Magnetic Resonance in Medicine / Society of Magnetic Resonance in Medicine*, Vol. 73, no. 2, pp. 843–850, 2015.

55. Cremillieux, Y., S. Ding, and J. F. Dunn, "High-resolution in vivo measurements of transverse relaxation times in rats at 7 Tesla," *Magnetic Resonance in Medicine*, Vol. 39, no. 2, pp. 285–290, 1998.

56. Behroozi, M., C. Chwiesko, F. Ströckens, M. Sauvage, *et al.*, "In vivo measurement of T1 and T2 relaxation times in awake pigeon and rat brains at 7T," *Magnetic Resonance in Medicine*, Vol. 79, no. 2, pp. 1090–1100, 2018.

57. Liachenko, S., and J. Ramu, "Quantification and reproducibility assessment of the regional brain T2 relaxation in naÃ¯ve rats at 7T," *Journal of Magnetic Resonance Imaging*, Vol. 45, no. 3, pp. 700–709, 2017.

58. Deruelle, T., F. Kober, A. Perles-Barbacaru, T. Delzescaux, *et al.*, "A Multicenter Preclinical MRI Study: Definition of Rat Brain Relaxometry Reference Maps," *Frontiers in Neuroinformatics*, Vol. 14, p. 22, 2020.

59. Karsa, A., S. Punwani, and K. Shmueli, "The effect of low resolution and coverage on the accuracy of susceptibility mapping," *Magnetic Resonance in Medicine*, Vol. 81, no. 3, pp. 1833–1848, 2019.

60. Kiersnowski, O. C., A. Karsa, S. J. Wastling, J. S. Thornton, *et al.*, "Investigating the effect of oblique image acquisition on the accuracy of QSM and a robust tilt correction method," *Magnetic Resonance in Medicine*, Vol. 89, no. 5, pp. 1791–1808, 2023.

61. Liu, T., P. Spincemaille, L. de Rochefort, B. Kressler, *et al.*, "Calculation of susceptibility through multiple orientation sampling (COSMOS): A method for conditioning the inverse problem from measured magnetic field map to susceptibility source image in MRI," *Magnetic Resonance in Medicine*, Vol. 61, no. 1, pp. 196–204, 2009.

62. Does, M. D., and J. C. Gore, "Compartmental study of T1 and T2 in rat brain and trigeminal nerve in vivo," *Magnetic Resonance in Medicine*, Vol. 47, no. 2, pp. 274–283, 2002.

63. Schofield, M. A., and Y. Zhu, "Fast phase unwrapping algorithm for interferometric applications," *Optics Letters*, Vol. 28, no. 14, pp. 1194–1196, 2003.

64. Schweser, F., A. Deistung, B. W. Lehr, and J. R. Reichenbach, "Quantitative imaging of intrinsic magnetic tissue properties using MRI signal phase: An approach to in vivo brain iron metabolism?," *NeuroImage*, Vol. 54, no. 4, pp. 2789–2807, 2011.

65. Li, W., A. V. Avram, B. Wu, X. Xiao, *et al.*, "Integrated Laplacian-based phase unwrapping and background phase removal for quantitative susceptibility mapping," *NMR in Biomedicine*, Vol. 27, no. 2, pp. 219–227, 2014.

66. Zhu, X., Y. Gao, F. Liu, S. Crozier, *et al.*, "BFRnet: A deep learning-based MR background field removal method for QSM of the brain containing significant pathological susceptibility sources," *Zeitschrift für Medizinische Physik*, Vol. 33, no. 4, pp. 578–590, 2023.

67. Hongyu, G., Z. Helong, and C. Hong, "Background field removal method of quantitative susceptibility mapping using deep learning," in *BIBE 2022; The 6th International Conference on Biological Information and Biomedical Engineering*, pp. 1–5, 2022.

68. Marques, J., and R. Bowtell, "Application of a Fourier-based method for rapid calculation of field inhomogeneity due to spatial variation of magnetic susceptibility," *Concepts in Magnetic Resonance Part B: Magnetic Resonance Engineering*, Vol. 25B, no. 1, pp. 65–78, 2005.